

See discussions, stats, and author profiles for this publication at: <https://www.researchgate.net/publication/230653776>

# Spectroscopy and Calculations for $4f(N) \rightarrow 4f(N-1)5d$ Transitions of Lanthanide Ions in $K_3YF_6$

ARTICLE in THE JOURNAL OF PHYSICAL CHEMISTRY A · AUGUST 2012

Impact Factor: 2.69 · DOI: 10.1021/jp306409p · Source: PubMed

CITATIONS

10

READS

110

5 AUTHORS, INCLUDING:



**Chong-Geng Ma**

Chongqing University of Posts and Telecomm...

60 PUBLICATIONS 319 CITATIONS

SEE PROFILE



**Mikhail G Brik**

University of Tartu

397 PUBLICATIONS 2,390 CITATIONS

SEE PROFILE



**Witold Ryba-Romanowski**

Polish Academy of Sciences

322 PUBLICATIONS 3,141 CITATIONS

SEE PROFILE



**H. C. Swart**

University of the Free State

470 PUBLICATIONS 2,803 CITATIONS

SEE PROFILE

# Spectroscopy and Calculations for $4f^N \rightarrow 4f^{N-1}5d$ Transitions of Lanthanide Ions in $K_3YF_6$

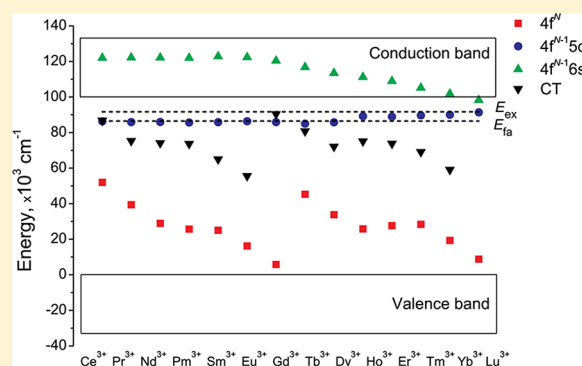
Chong-Geng Ma,<sup>†</sup> Mikhail G. Brik,<sup>\*,†</sup> Witold Ryba-Romanowski,<sup>‡</sup> Hendrik C. Swart,<sup>§</sup> and Marek A. Gusowski<sup>\*,§</sup>

<sup>†</sup>Institute of Physics, University of Tartu, Riia 142, 51014 Tartu, Estonia

<sup>‡</sup>Department of Laser Materials Spectroscopy, Trzebiatowski Institute of Low Temperature and Structure Research, Polish Academy of Sciences, P.O. Box 1410, 50-950 Wrocław, Poland

<sup>§</sup>Department of Physics, Faculty of Natural and Agricultural Sciences, University of the Free State, Nelson Mandela Drive (IB 51), P.O. Box 339, Bloemfontein 9300, South Africa

**ABSTRACT:** In the present work, we report on the combined experimental and theoretical studies of the  $4f$ – $5d$  spectra of  $Ce^{3+}$ ,  $Pr^{3+}$ ,  $Nd^{3+}$ ,  $Eu^{3+}$ ,  $Gd^{3+}$ ,  $Tb^{3+}$ ,  $Dy^{3+}$ , and  $Er^{3+}$  ions in a newly synthesized  $K_3YF_6$  matrix. The low temperature experimental  $4f$ – $5d$  excitation spectra have been analyzed and compared with the results of the energy-level and intensity calculations. For this theoretical analysis, the extended phenomenological crystal-field model for the  $4f^{N-1}5d$  configuration (i.e., the extended  $f$ -shell programs, developed by Prof. M. F. Reid) and exchange charge model (developed by Prof. B. Z. Malkin) have been used together to estimate the crystal field parameters and implement the spectral simulations. On the basis of the results of the performed theoretical analysis, we suggest the most probable positions occupied by optically active ions. Although the spectra of only eight lanthanide ions have been studied, the Hamiltonian parameters of the  $4f^{N-1}5d$  configuration have been evaluated for the whole lanthanide series and reported here for the first time, to give a complete and unified description of the spectroscopic properties of the trivalent rare earth ions in the chosen host. In addition to the studies of the  $4f$ – $5d$  transitions, various possible competitive excitation channels overlapping with  $4f$ – $5d$  ones have also been discussed, where a theoretical scheme giving rudiments to understand  $4f$ – $6s$  spectra are proposed for the first time. An excellent agreement between the calculated and measured excitation spectra shapes confirms validity of the performed analysis. The obtained parameters of the crystal field Hamiltonians for different ions and various electron configurations can be used in a straightforward way to generate the energy level positions and calculate the particular transition intensities for any rare earth ion in any particular spectral region. With the aid of the obtained parameters, the positions of the lowest energy levels of the  $4f^N$ ,  $4f^{N-1}5d$ , and  $4f^{N-1}6s$  configurations of rare earth ions and  $4f^{N+1}(np)^5$  configuration of rare earth ions and ligands (corresponding to the ligand–impurity ion charge transfer transitions) in the band gap of  $K_3YF_6$  have all been estimated. The obtained Hamiltonian parameters and energy levels diagrams, which include the electronic structure of a host material, can be used as a starting point for analysis of spectroscopic properties of trivalent lanthanides in similar fluorides.



## INTRODUCTION

The last decades have brought along the increased interests in new solid state luminescent materials operating in the ultraviolet (UV) and vacuum ultraviolet (VUV) range. It is generated by the requirement of wide applications of UV lasers and fast scintillators as well as the need of replacing conventional phosphors with luminescent materials, which can be applied in mercury-free fluorescent lamps, plasma display panels, etc.<sup>1–8</sup> This tendency has triggered the desire to expand the fundamental knowledge of the high-energy  $4f^{N-1}5d$  states and  $4f^N \leftrightarrow 4f^{N-1}5d$  (i.e.,  $4f$ – $5d$ ) transitions of lanthanide ions in solids. Many high-resolution  $4f$ – $5d$  transition spectra of trivalent lanthanide ions ( $Ln^{3+}$ ) have been reported in a number of fluoride crystals due to their larger band gaps. A

detailed overview of them has recently been provided in the introduction part of ref 9.

Recently, the newly synthesized  $K_3YF_6$  crystal doped with  $Ln^{3+}$  ions ( $Ln = Nd$  or  $Tb$ )<sup>10–12</sup> as a new VUV material has attracted more attention. One of the reasons is the fact that it possesses low-energy phonons (with the energy not exceeding  $463\text{ cm}^{-1}$ ), which can play a crucial role in the  $5d$ – $4f$  emission efficiency associated with the multiphonon nonradiative relaxation process between the higher and lowest  $4f^{N-1}5d$  energy states. Another reason is the possible presence of several available sites for  $Ln^{3+}$  ions in this system since Schiffbauer et

Received: June 29, 2012

Revised: August 8, 2012

Published: August 10, 2012

al.<sup>13</sup> have reported that  $\text{Pr}^{3+}$  ions can occupy three sites ( $\text{Cs}^+$ ,  $\text{K}^+$ , and  $\text{Y}^{3+}$ ) in the  $\text{Cs}_2\text{KYF}_6$  host being very similar to the present studied one. The solution to this question will facilitate the understanding of the 4f–5d spectra of  $\text{Ln}^{3+}$  ions simultaneously located at many different sites.<sup>14–16</sup> Moreover, it can help answer a question whether unclear features of the 4f–5d spectra of  $\text{Ln}^{3+}$  with a larger ionic radius (mainly, the light lanthanide ions) can be accounted for by the presence of a second different ionic site in a phase or a second phase with the replacement of the same host cation, such as those of  $\text{Ce}^{3+}$  and  $\text{Pr}^{3+}$  ions in  $\text{Cs}_2\text{NaYF}_6$ .<sup>9</sup> In addition, it is very interesting to make a complete 4f–5d spectral study across the whole lanthanide series in this host, which may have a significant contribution to the knowledge of VUV optical properties of  $\text{Ln}^{3+}$  ions in the fluoride family.

A theoretical study of the highly excited  $4f^{N-1}5d$  energy states is beneficial to the prediction of the performance of such VUV materials. Thus, in 2000, the semiempirical calculations of energy levels for the  $4f^N$  configuration<sup>17,18</sup> were successfully extended to the  $4f^{N-1}5d$  configuration by Reid et al.,<sup>19</sup> and then, extensive calculations have been applied to almost the whole lanthanide series in  $\text{CaF}_2$ ,  $\text{LiYF}_4$ ,  $\text{YPO}_4$ , and  $\text{Cs}_2\text{NaYX}_6$  ( $\text{X} = \text{F}$  and  $\text{Cl}$ ),<sup>9,20–23</sup> which have given satisfactory theoretical results that were in agreement with the experimental results. The extended phenomenological crystal-field (CF) model requires many parameters to give an electronic structure with thousands of energy levels. Among these parameters, the 5d crystal field parameters (CFPs) are strongly host-dependent and usually determined from the 4f–5d absorption or excitation spectra of  $\text{Ce}^{3+}$  by the least-squares fitting and extrapolated to ions across the lanthanide series.<sup>20,21</sup> For high symmetry sites, such a determination due to a small number of the fitting parameters is easy, and the model works very well, as shown by the theoretical studies mentioned before. However, for sites with very low symmetry, such as  $C_i$  or  $C_1$ , the model fails in the simulations because the estimation of the 5d CFPs through the energy-level fitting becomes almost impossible due to the fact that the number of the 5d CFPs is greater than that of the possibly observed bands. Such a circumstance considerably limits the application of the extended CF model to the low symmetry system.

In the VUV energy region of the  $\text{Ln}^{3+}$  ions in the hosts, various excitation channels including the host absorption, charge transfer (CT), and  $4f^N \rightarrow 4f^{N-1}6s$  (i.e., 4f–6s) transitions compete with the 4f–5d transitions. Dorenbos<sup>24–27</sup>

has used the diagram for the lowest 4f, 5d, and CT energy positions of ions across the whole lanthanide series relative to the valence and conduction bands to understand all the above transitions except the 4f–6s ones based on the empirical formulas proposed by himself. The application of such diagram to  $\text{K}_3\text{YF}_6$  host will be attractive and can form a thorough understanding of the VUV spectra of ions across the series in this host. However, the 4f–6s transition has not been included in such a diagram yet. Furthermore, no theoretical study about this transition has been carried out up to now, although the 4f–6s absorptions or excitations of  $\text{Ce}^{3+}$  and  $\text{Pr}^{3+}$  ions have been measured and assigned in many fluoride hosts, such as  $\text{LaF}_3$ ,  $\text{CeF}_3$ ,  $\text{LuF}_3$ ,  $\text{LiYF}_4$ , and  $\text{LiLuF}_4$ .<sup>28–31</sup> Therefore, it is very meaningful to propose an empirical model like Dorenbos's for the 4f–6s transition.

On the basis of the above challenges in both theory and experiment, the present work aims at a systematic study of the 4f–5d transitions of  $\text{Ln}^{3+}$  ions in the  $\text{K}_3\text{YF}_6$  host and other

competitive transitions overlapping with the 4f–5d ones by widely employing all the present theoretical means and their extensions developed by us. This article is organized as follows: in the Experimental Details section, we have described the details about the sample preparations and the spectral measurements. In the Theory section, the combined theory to perform the 4f–5d spectral simulations of  $\text{Ln}^{3+}$  ions in crystals and to evaluate all of the CF parameter values for any site has been presented based on the extended CF model for the  $4f^{N-1}5d$  configuration<sup>19</sup> and exchange charge model (ECM).<sup>32</sup> Then, the other excitation channels competing with the 4f–5d transition have also been theoretically discussed and schematically shown within the host band structure and, especially, an empirical formula to evaluate the 4f–6s transition energy has been proposed for the first time. In the Comparison section, we have applied the theoretical results from the Theory section to the interpretations of the excitation spectra of eight  $\text{Ln}^{3+}$  ions in the  $\text{K}_3\text{YF}_6$  host. Finally, Conclusions have been presented.

## ■ EXPERIMENTAL DETAILS

The polycrystalline samples containing  $\text{Ln}^{3+}$  ions were prepared by roasting the stoichiometric mixture of nominally anhydrous  $\text{KF}$ ,  $\text{YF}_3$ , and  $\text{LnF}_3$  (Sigma) with 2%  $\text{NH}_4\text{F}\cdot\text{HF}$  admixture. The reagents were put into a platinum crucible and covered by a platinum cup. Prior to purging by Ar, the growth chamber was evacuated to  $10^{-2}$  Pa and heated to 300 °C for a period of 5 h. Such a treatment was carried out to eliminate residual water and/or oxygen impurities from the chamber and the starting materials. The synthesis was carried out at 1000 °C for 20 h with the insignificant Ar overpressure, then the sample was cooled down to room temperature with a 0.5 °C/min pace. In this manner, samples of  $\text{K}_3\text{YF}_6\text{:Ln}^{3+}$  have been prepared. Samples were checked for phase purity by recording X-ray powder diffractograms using a STOE X-ray diffractometer, with image plate, counter, and program STOE Win XPOW v. 2.11, and found to be single phase.

$\text{K}_3\text{YF}_6$  has the cryolite-type monoclinic structure (space group  $P2_1/n$ , 1401), which is composed of distorted  $\text{YF}_6$  and  $\text{K}(1)\text{F}_6$  octahedras and  $\text{K}(2)\text{F}_4$  tetrahedra (here  $\text{K}(1)$  and  $\text{K}(2)$  symbols stand for two different sites of K ions). The Y and  $\text{K}(1)$  ions both have  $C_i$  site symmetry, whereas the  $\text{K}(2)$  ion occupies a general position with  $C_1$  site symmetry.

More details concerning the structural investigation and analysis of lattice vibrations of  $\text{K}_3\text{YF}_6$  can be found in our earlier paper.<sup>10</sup> The present measurements for phase purity show that small amounts of  $\text{Ln}^{3+}$  ions doped into this crystal do not change the local structure and affect the crystal structure stability. After doping, the  $\text{Ln}^{3+}$  ions generally occupy the  $\text{Y}^{3+}$  sites due to their similar chemical properties, but it is possible that some of them also go into  $\text{K}^+$  sites being of larger size (for example,  $r(\text{K}^+(1)) = 1.38$  Å) followed by the necessary charge compensation. This is probable as the ionic radii of the majority of the  $\text{Ln}^{3+}$  ions are much larger than those of  $\text{Y}^{3+}$  ions ( $r(\text{Y}^{3+}) = 0.9$  Å) as shown in the Table 1 where all the data of the ionic radii of various cations involved in the system  $\text{K}_3\text{YF}_6\text{:Ln}^{3+}$  are collected from ref 33. The present hypothesis is not groundless and has already been found valid in some materials, such as  $\text{KMgF}_3\text{:Ce}^{3+}$ .<sup>16</sup> In addition, the  $\text{K}(1)$  sites rather than the  $\text{K}(2)$  sites are preferred due to high coordination number.

High-resolution excitation spectra were recorded at the Deutsches Elektronen Synchrotron (DESY, Hamburg, Germany) using the facility of SUPERLUMI station at

**Table 1. Ionic Radii of Various Cations Involved in the System  $K_3YF_6:Ln^{3+}$  (unit, Å)**

cation	ionic radius	cation	ionic radius
Ce <sup>3+</sup>	1.01	Ho <sup>3+</sup>	0.901
Pr <sup>3+</sup>	0.99	Er <sup>3+</sup>	0.89
Nd <sup>3+</sup>	0.983	Tm <sup>3+</sup>	0.88
Pm <sup>3+</sup>	0.97	Yb <sup>3+</sup>	0.868
Sm <sup>3+</sup>	0.958	Lu <sup>3+</sup>	0.861
Eu <sup>3+</sup>	0.947	Y <sup>3+</sup>	0.9
Gd <sup>3+</sup>	0.938	K <sup>+</sup> (1) <sup>a</sup>	1.38
Tb <sup>3+</sup>	0.923	K <sup>+</sup> (2) <sup>a</sup>	1.37
Dy <sup>3+</sup>	0.912		

<sup>a</sup>For K<sup>+</sup> ion, the ionic radii have two different values due to the different coordination numbers of the K(1) and K(2) sites in  $K_3YF_6$  host.

HASYLAB.<sup>34</sup> The excitation spectra were recorded at temperature 8 K with resolution about 0.3 nm, the spectra were corrected for the spectral distribution of the synchrotron radiation intensity using reference sample of sodium salicylate whose quantum efficiency is constant over the excitation wavelength range.<sup>35</sup>

## THEORY

### Parameterized CF Model of $4f^{N-1}5d$ Configuration.

The effective Hamiltonian for the  $4f^{N-1}5d$  configurations of lanthanide ions in crystals generally consists of three parts: the interactions within the  $4f^{N-1}$  core, for 5d single electron, and interaction between the 4f and 5d electrons, and thus can be written as

$$\mathcal{H}(4f^{N-1}5d) = \mathcal{H}(ff) + \mathcal{H}(dd) + \mathcal{H}(fd) \quad (1)$$

where the first and last terms will not exist for  $N = 1$  because there only appears  $5d^1$  excited configuration. The above three terms can be further expressed, respectively, as shown below:

$$\begin{aligned} \mathcal{H}(ff) = & \sum_{k=2,4,6} F^k(ff)f_k + \zeta_f(f)A_{so} + \alpha(ff)L(L+1) \\ & + \beta(ff)G(G_2) + \gamma(ff)G(G_7) + \sum_{i=2,3,4,6,7,8} T^i(ff)t_i \\ & + \sum_{h=0,2,4} M^h(ff)m_h + \sum_{k=2,4,6} P^k(ff)p_k \\ & + \sum_{k=2,4,6;q=-k,\dots,k} B_q^k(f)C_q^{(k)} \end{aligned} \quad (2)$$

$$\mathcal{H}(dd) = \sum_{k=2,4;q=-k,\dots,k} B_q^k(d)C_q^{(k)} + \zeta_d(d)A_{so(d)} \quad (3)$$

$$\mathcal{H}(fd) = \sum_{k=2,4} F^k(fd)f_k + \sum_{j=1,3,5} G^j(fd)g_j + \Delta_E(fd) \quad (4)$$

where the notation and meanings of various operators and parameters are defined according to the standard practice.<sup>17–19</sup> It is noted that the three body operator  $t_i$  can effectively contribute only when  $3 < N < 13$ , and for  $N = 2$  or  $N = 14$ , there are only the spin–orbit and CF interactions in eq 2.

The energy level calculation of the  $4f^N$  configuration also needs to be simultaneously implemented with that of  $4f^{N-1}5d$  configuration because the 4f–5d transition energies between the ground state of the  $4f^N$  configuration and  $4f^{N-1}5d$  energy levels are actually the sum of the barycenter energy of the  $4f^N$

configuration and the eigenvalues of the effective Hamiltonian for the  $4f^{N-1}5d$  configuration. The standard and proven technique for the  $4f^N$  energy level calculation can be adopted, as shown in ref 17, and the effective Hamiltonian of the  $4f^N$  configuration is almost the same as eq 2 except that one additional parameter  $E_{avg}$  is introduced to shift all the  $4f^N$  energy levels so that the energy of the lowest level of  $4f^N$  is zero.

### Determination of Parameter Values and Simulation of Spectra. $4f^N$ Configuration Parameters.

Many systematic determinations of  $4f^N$  parameters for ions across the lanthanide series have been carried out in some hosts with relatively higher site symmetries, such as  $LaF_3$ ,<sup>17</sup>  $YOCl_6$ ,<sup>36</sup> and  $Cs_2NaYCl_6$ ,<sup>37</sup> by the general least-squares fitting. However, to the best of our knowledge, there are no available observed information to be used to determine the  $4f^N$  parameter values of rare earth ions in the present  $K_3YF_6$  host. Moreover, the  $C_i$  site symmetry of doped  $Ln^{3+}$  ions in this crystal can hardly reduce the number of CFPs of the 4f electrons, which may result in the possible failure of the fitting procedure. Thus, it is necessary to make some reasonable estimations for the  $4f^N$  parameters rather than fitting observed data. Since the  $4f^N$  quasi-free ion parameters can be approximately regarded as constant for a given ion in different hosts, these quasi-free ion parameter values will be directly taken from those in the  $LaF_3$  host tabulated by Carnall et al.<sup>17</sup> Concerning the CFPs of  $4f^N$  configuration for ions across the lanthanide series, those of  $Eu^{3+}$  ion will be first determined and compared with those known values in other hosts with similar local structure to verify the validity of our estimation due to a role of  $Eu^{3+}$  ion as a probe of local site environment, and any CFP of another ion can also be estimated by scaling the corresponding CFP of  $Eu^{3+}$  ion by the ratio (denoted as  $\eta_{cf}(f)$ ) of the CF strength<sup>38</sup> of this ion to  $Eu^{3+}$  ion in  $LaF_3$  host.<sup>17,39</sup> The direct evaluation of CFPs of  $Eu^{3+}$  ion is implemented by applying the ECM<sup>32</sup> where the usage of the crystal structure data can effectively show a deeper understanding of CFPs. More calculation details of CFPs can be found in the next section. After calculating the energy splittings of the  $4f^N$  configuration by employing the above parameter values,  $E_{avg}$  parameter values will be determined naturally.

**$4f^{N-1}5d$  Configuration Parameters.** Since hundreds or thousands of electronic transition zero-phonon lines (ZPLs) between the two configuration  $4f^N$  and  $4f^{N-1}5d$  are generally convolved into several to a few dozens of broad bands in measured f–d absorption or excitation spectra, the f–d transition spectra are not sensitive to all the  $4f^{N-1}5d$  parameters. The  $4f^{N-1}$  core parameters are almost exactly like that, and thus, the same parameter values as for the  $4f^N$  configuration can be used for the  $4f^{N-1}$  core. It is noted that some parameters for the  $4f^{N-1}$  core possibly due to nonexistence of the similar parameters for the  $4f^N$  configuration have to be extrapolated from the previous ion in the lanthanide series by following the empirical method proposed by Duan et al.<sup>40,41</sup> In addition, to slightly characterize the contraction of the 4f orbitals within the  $4f^{N-1}$  core relative to the  $4f^N$  configuration, we enlarged the strong Coulomb parameters  $F^k(ff)$  ( $k = 2,4,6$ ) and spin–orbit coupling parameter  $\zeta_f(f)$  of the  $4f^{N-1}$  core from those existent values for the  $4f^N$  configuration by the ab initio ratio 1.06 derived from ref 42, as was done by van Pieterse et al. in refs 20 and 21.

The insensitive 5d spin–orbit parameter values can almost not be varied and fixed at those standard Hartree–Fock values listed in ref 42. The estimation of the 5d CFPs for the low



symmetry site is usually not easy as mentioned in the Introduction. In general, there are two kinds of much better methods to overcome such difficulty: the first one is extracting CFPs from ab initio calculations as Reid et al. have recently proposed,<sup>43,44</sup> and the second one is trying to reduce the number of CFPs as much as possible by keeping some ratios or relations between CFPs so that the fitting calculation for  $\text{Ce}^{3+}$  spectra can go on. Although the former can give qualitatively reasonably accurate results, the calculation time costs are great as we know. In this work, the ECM belonging to the latter was adopted, where there are only 1–3 independent adjustable parameters.<sup>32</sup> Thus, the 5d CFPs for  $\text{Ce}^{3+}$  ions will be optimized from the 5d CF splitting shown in the f–d transition spectra based on the ECM, and then, they were appropriately reduced for  $\text{Ln}^{3+}$  ion by multiplying a small linear ratio (denoted as  $\eta_{\text{cf}}(\text{d})$ ) of the 5d CF strength of this ion to that of the  $\text{Ce}^{3+}$  ion in the  $\text{LiYF}_4$  host.<sup>20,21</sup> It is noted that the reduction of 5d CFPs was not taken into account for the light  $\text{Ln}^{3+}$  ions in the calculations of van Pieterse et al.,<sup>20</sup> and thus, the obtained linear trend for heavy  $\text{Ln}^{3+}$  ions plotted in Figure 1 had to be extrapolated to light ones.

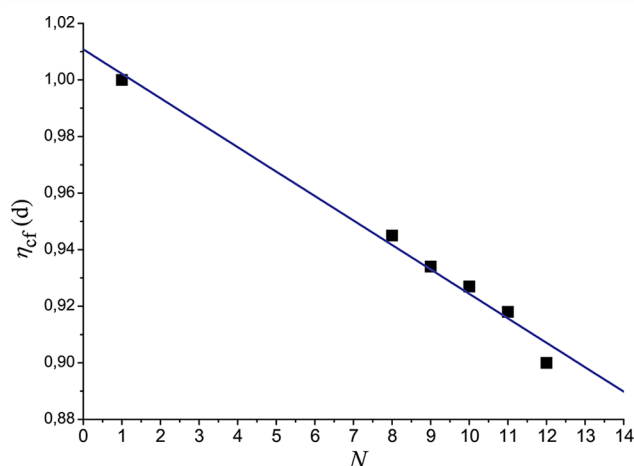


**Figure 1.** Variation trend of  $\eta_{\text{cf}}(\text{d})$  (the ratio of the 5d CF strength of any ion to that of the  $\text{Ce}^{3+}$  ion in the  $\text{LiYF}_4$  host) against electron number of  $4f^{N-1}5d$  configuration  $N$ . The linear fitting equation for  $\eta_{\text{cf}}(\text{d})$  is  $1.01 - 0.01N$ .

The direct and exchange Coulomb parameters between 4f and 5d electrons (i.e.,  $F^k(\text{fd})$  ( $k = 2, 4$ ) and  $G^j(\text{fd})$  ( $j = 1, 3, 5$ ) for free ions are tabulated in ref 42. An additional reduction in these parameters for ions in crystals will be necessary and expected due to the well-known nephelauxetic effect,<sup>45</sup> which causes the 5d orbitals to be partly delocalized over the ligands, reducing the interaction with the 4f core. The scaling ratio  $\eta_{\text{fd}}$  for these parameters was directly optimized from the splitting between the high- and low-spin (HS and LS) states of the  $\text{Tb}^{3+}$  ions in the  $\text{K}_3\text{YF}_6$  host, and then fixed at the value 0.61 for  $\text{Pr}^{3+}$  and following ions. After all the above parameters were fully determined, the parameter  $\Delta_{\text{E}}(\text{fd})$ , which shifts all  $4f^{N-1}5d$  energy levels by the same amount will be adjusted to obtain the best agreement between experimental and calculated energy levels. The parameter  $\Delta_{\text{E}}(\text{fd})$  values for eight measured  $\text{Ln}^{3+}$  ions in  $\text{K}_3\text{YF}_6$  were fitted with a second-order polynomial using  $N$  (the number of electrons in the  $4f^{N-1}5d$  configuration) as the variable in Figure 2, and those for other ions not measured can be extrapolated from the theoretical fitting curve. All the

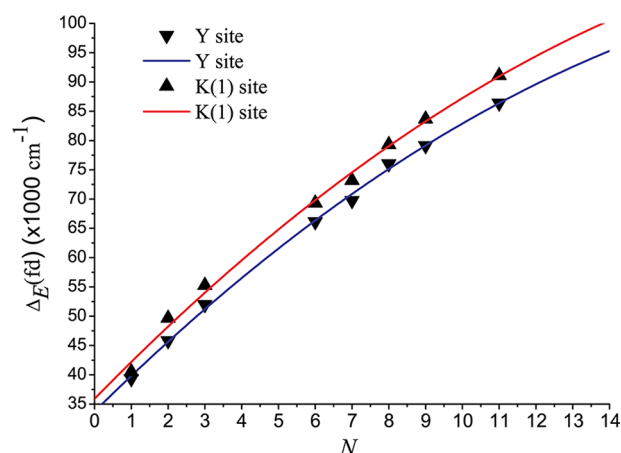


**Figure 2.** Energy differences between the barycenters of the  $4f^{N-1}5d$  and  $4f^N$  configuration of  $\text{Ln}^{3+}$  ions, respectively, situated at the Y and K(1) sites in the  $\text{K}_3\text{YF}_6$  host. The fitting equations with a second-order polynomial for the Y and K(1) sites are, respectively,  $33.73 + 6.21N - 0.13N^2$  and  $35.89 + 6.43N - 0.13N^2$  (unit,  $10^3 \text{ cm}^{-1}$ ).

parameters and their values for ions across the lanthanide series used in the energy level calculations are listed in Table 2.

**Simulation of Vibronic Bands.** In addition to  $4f^{N-1}5d$  energy level calculations, the 4f–5d electric-dipole transition intensities also need to be evaluated to characterize the intensities of the vibronic bands. These calculations are very straightforward by employing eq 28 in ref 46 after the multielectron wavefunctions of  $4f^N$  and  $4f^{N-1}5d$  are obtained by diagonalizing the effective parametrized Hamiltonian matrices for two configurations. As mentioned before, the majority of the 4f–5d transition ZPLs is buried in vibronic bands because there is generally a displacement between the equilibrium positions of ligands in the excited and ground configuration states due to very strong coupling interactions between the 5d orbitals and the lattice. For such broad band structures of the f–d spectra, there have been some theoretical attempts to treat them in more detail,<sup>47,48</sup> but only the vibronic bands with fine structures can be well simulated. According to the not well-resolved features of the present measured 4f–5d spectra, we adopted the model proposed by Reid et al.,<sup>19–21</sup> where the areas beneath the vibronic bands are proportional to the 4f–5d transition line strengths, and the vibronic bands in the 4f–5d excitation spectra are reproduced by using the Gaussian shaped curves with a full width  $E_{\text{width}}$  at half-maximum (fwhm), displaced from the zero-phonon lines toward higher energy by  $E_{\text{shift}}$ . Values used in the present calculations were  $E_{\text{shift}} = 1170 \text{ cm}^{-1}$  and  $E_{\text{width}} = 1520 \text{ cm}^{-1}$ . The former can be directly taken from half of the Stokes shift for the 4f–5d transition of  $\text{Nd}^{3+}$  ions in the  $\text{K}_3\text{YF}_6$  host, previously reported in ref 11. If only the totally symmetric  $A_{1g}$  vibrational mode for the  $\text{YF}_6^{3-}$  moiety with the energy of  $463 \text{ cm}^{-1}$  obtained from Raman spectra of  $\text{K}_3\text{YF}_6$ <sup>10</sup> was considered in this simulation, the Huang–Rhys factor  $S$  can be determined to be about 2.52, which is very close to the value (i.e., 2.5) in  $\text{CaF}_2$  host.<sup>20</sup> The latter was estimated directly from the first 4f–5d excitation band of  $\text{Ce}^{3+}$  ions in  $\text{K}_3\text{YF}_6$ . All the above calculations or simulations employed the extended f-shell programs written by M. F. Reid.

**Crystal Field Parameter Calculation Based on the ECM.** *Theory Descriptions of ECM.* The ECM proposed by B. Z. Malkin<sup>32</sup> has been successfully applied to the modeling of

Table 2. Parameters Employed in the Energy Level Calculations for  $4f^N$  and  $4f^{N-1}5d$  Configurations of  $L_n^{3+}$  Ions, Respectively, Situated at the Y and K(1) Sites in  $K_2YF_6$ <sup>a</sup>

	parameter <sup>b</sup>	Ce <sup>3+</sup>	Pt <sup>3+</sup>	Nd <sup>3+</sup>	[Pm <sup>3+</sup> ]	[Sm <sup>3+</sup> ]	Eu <sup>3+</sup>	Gd <sup>3+</sup>	Tb <sup>3+</sup>	Dy <sup>3+</sup>	[Ho <sup>3+</sup> ]	Er <sup>3+</sup>	[Tm <sup>3+</sup> ]	[Yb <sup>3+</sup> ]	[Lu <sup>3+</sup> ]
4f <sup>N-1</sup> core	F <sup>2</sup> (f)			77399	80984	84593	88113	90809	94335	97417	100238	103332	106142	107744	
	F <sup>4</sup> (f)			55956	58194	60606	62824	64475	66694	68234	70381	71978	73790	74904	
	F <sup>6</sup> (f)			37902	39962	42665	45114	47463	50087	52349	55143	57251	59334	60229	
	ζ <sub>f</sub> (f)		796.8	938.4	1086.5	1246.6	1418.3	1598.5	1809.4	2027.8	2273.7	2518.6	2794.2	3103.7	3381.8
	α(f)			21.34	20.50	20.16	20.16	18.92	18.40	18.02	17.15	17.79	17.26	17.26	
	β(f)			−593.0	−560	−566.9	−566.9	−600	−590.9	−633.4	−607.9	−582.1	−624.5	−624.5	
	γ(f)			1445	1475	1500	1500	1575	1650	1790	1800	1800	1820	1820	
	T <sup>2</sup> (f)				300	300	300	300	320	329	400	400	400	400	
	T <sup>3</sup> (f)				35	36	40	42	40	36	37	43	43	43	
	T <sup>4</sup> (f)				58	56	60	62	50	127	107	73	73	73	
5d	T <sup>6</sup> (f)				−310	−347	−300	−295	−395	−314	−264	−271	−271	−271	
	T <sup>7</sup> (f)				350	373	370	350	303	404	316	308	308	308	
	T <sup>8</sup> (f)				320	348	320	310	317	315	336	299	299	299	
	M <sup>0</sup> (f) <sup>d</sup>			2.11	2.4	2.60	2.1	3.22	2.39	3.39	2.54	3.86	3.81	3.81	
	P <sup>2</sup> (f) <sup>d</sup>			192	275	357	360	676	373	719	605	594	695	695	
	η <sub>d</sub> (f)	1.15 <sup>e</sup>	1.16	1.11	1.04	1.02	1.00	0.85	0.85	0.82	0.80	0.74	0.73	0.73	0.73 <sup>e</sup>
	ζ <sub>d</sub> (d)	1082	1149	1216	1283	1351	1419	1488	1557	1627	1697	1768	1839	1910	1982
	η <sub>d</sub> (d)	1.00	0.99	0.99	0.98	0.97	0.96	0.95	0.94	0.93	0.93	0.92	0.90	0.90	0.89
	η <sub>ld</sub>	0.61	0.61	0.61	0.61	0.61	0.61	0.61	0.61	0.61	0.61	0.61	0.61	0.61	0.61
	Δ <sub>E</sub> (fd, Y)	39332	45816	51975	56509	61555	66122	69753	76025	79119	82892	86383	89610	92580	95290
4f–5d	Δ <sub>E</sub> (fd, K(1))	40536	49660	55265	59540	64804	69321	73192	79315	83663	87236	91106	94394	97584	100515
4f <sup>Nc</sup>	E <sub>avg</sub> (Y)	1966	10619	24603	37291	47979	64089	87802	68812	56496	48723	35850	17836	4856	0
	E <sub>avg</sub> (K(1))	1457	10054	24317	37026	47730	63993	87802	68575	56260	48499	35674	17539	4507	0

<sup>a</sup>Detailed explanations and determinations of these parameters can be found in the text. Units of the energy parameters are in cm<sup>−1</sup>. <sup>b</sup>The parameters without the labeling of site name can be applied to any site. The parameter values belonging to those  $L_n^{3+}$  ions labeled in the square brackets are obtained from the prediction of the empirical method proposed in the theory section. <sup>c</sup>The quasi-free ion parameter values for 4f<sup>N</sup> configuration are not tabulated for the sake of brevity, and one can find them in ref 17. The CFPs for 4f<sup>N</sup> configuration are the same as those for 4f<sup>N-1</sup> core. <sup>d</sup>M<sup>0</sup>(f)/M<sup>0</sup>(f) = 0.56, M<sup>1</sup>(f)/M<sup>0</sup>(f) = 0.38, P<sup>4</sup>(f)/P<sup>2</sup>(f) = 0.75, and P<sup>6</sup>(f)/P<sup>2</sup>(f) = 0.5 were used to constrain those corresponding parameters not listed in the table. <sup>e</sup>There are no 4f CFPs for 5d<sup>1</sup> configuration of Ce<sup>3+</sup> ion and no 4f CFPs for 4f<sup>14</sup> configuration of Lu<sup>3+</sup> ion.

the even or odd parity CF interactions of  $f^{49-54}$  and  $d^{48,52,55-58}$  electrons of rare earth ions in various crystals. Here, a brief description of this model is first given by following the notations used in ref 59 by G. K. Liu, and then more attention will be paid to its application to our present  $K_3YF_6$  host.

In the framework of ECM, the CFPs of 4f and 5d electrons uniformly denoted as  $B_q^k(nl)$  ( $nl = 4f$  or  $5d$ ) (i.e., the expressions of CFPs in eqs 2 and 3) can be written as a sum of two different contributions:

$$B_q^k(nl) = B_q^{(pc)k}(nl) + B_q^{(ec)k}(nl) \quad (5)$$

where  $B_q^{(pc)k}(nl)$  and  $B_q^{(ec)k}(nl)$  represent the contributions of point charges of all the crystal lattice ions and introduced fictitious exchange charges due to the spatial distribution of ligand electron density, respectively, as shown below:

$$B_q^{(pc)k}(nl) = -e^2 \langle nllr^k | nl \rangle \sum_i q_i \beta_k \times (-1)^k C_{-q}^k(\theta_i, \varphi_i) / R_i^{k+1} \quad (6)$$

$$B_q^{(ec)k}(nl) = e^2 \frac{2(2k+1)}{2l+1} \sum_L S_k^{nl}(R_L) \times (-1)^k C_{-q}^k(\theta_L, \varphi_L) / R_L \quad (7)$$

Here,  $C_{-q}^k$  is the spherical function with rank  $k$  and order  $-q$  defined by Wybourne,<sup>18</sup> the index  $i$  and  $L$  are, respectively, used to enumerate all the crystal lattice ions and the ligand ions in the nearest-neighbor coordination shell, and  $(R_i, \theta_i, \varphi_i)$  and  $(R_L, \theta_L, \varphi_L)$  are, respectively, spherical coordinates of the  $i$ th crystal lattice ions with the net charge  $eq_i$  and the  $L$ th ligand ions in the reference system centered at the  $Ln^{3+}$  ions. For the first term in eq 5,  $\langle nllr^k | nl \rangle$  is the radial integral of  $r^k$  between  $nl$  orbitals of the  $Ln^{3+}$  ion and can be either obtained from literature or numerically calculated using the radial wavefunctions of the corresponding ion; the reduction factor  $\beta_k$  ( $k = 2 \cdots 2l$ ) is defined as 1 minus the shielding constant  $\sigma_k^{60}$  (i.e.,  $1 - \sigma_k$ ) for the 4f electrons due to the screening effects of the 4f electrons by the outer  $5s^2 5p^6$  shell, but for 5d electrons, it actually accounts for extended charge distributions of a 5d electron and its ligands' outer electrons, and can be evaluated by using the bipolar expansion proposed in the ref 61. The last exchange charge term is directly proportional to the following quadratic forms of various overlap integrals between  $nl$  orbitals of the central  $Ln^{3+}$  ion and the outer  $n'p$  and  $n's$  orbitals of the ligands:

$$S_k^{nl}(R_L) = G_s^{nl} S_s^{nl}(R_L)^2 + G_\sigma^{nl} S_\sigma^{nl}(R_L)^2 + \gamma_k^{nl} G_\pi^{nl} S_\pi^{nl}(R_L)^2 \quad (8)$$

where  $\gamma_2^{4f} = 3/2$ ,  $\gamma_4^{4f} = 1/3$ ,  $\gamma_6^{4f} = -(3/2)$ ,  $\gamma_2^{5d} = 1$ , and  $\gamma_4^{5d} = -(4/3)$ ;  $S_s^{nl}(R_L) = \langle nl0|n's0 \rangle$ ,  $S_\sigma^{nl}(R_L) = \langle nl0|n'p0 \rangle$ , and  $S_\pi^{nl}(R_L) = \langle nl \pm 1|n'p \pm 1 \rangle$  (here, the  $nlm$  notation is employed, where  $n$ ,  $l$ , and  $m$  are, respectively, the principle, orbital, and magnetic quantum numbers); the  $G_s^{nl}$ ,  $G_\sigma^{nl}$ , and  $G_\pi^{nl}$  entries are the dimensionless adjustable parameters, whose values are determined from the experimental spectra.

**Determination of CFPs in  $K_3YF_6$ .** According to the descriptions of the determinations of CFPs of 4f and 5d electrons in the previous section, the CFP calculations will focus on 5d CFPs of  $Ce^{3+}$  ions and 4f CFPs of  $Eu^{3+}$  ions. Before applying the ECM eqs 6 and 7, the following preparation works have been implemented. First, the moments of the 5d-electron density and the overlap integrals between

$Ce^{3+}$  and  $F^-$  ions for various interionic distances were numerically calculated by using the analytical radial 5d wavefunctions of  $Ce^{3+}$  ions presented in ref 62, and the 2s and 2p wavefunctions of  $F^-$  ions are taken from ref 63. Figure 3

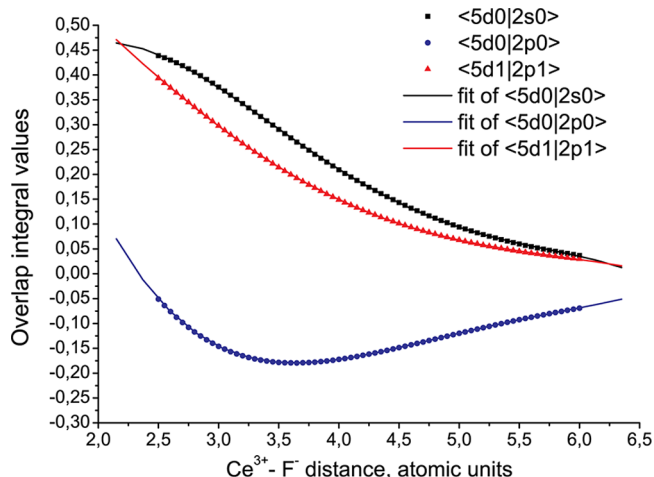


**Figure 3.** Calculated dependence of overlap integrals on the distance between  $Ce^{3+}$  and  $F^-$  ions ( $\square$ ,  $\langle 5d0|2s0 \rangle$ ;  $\circ$ ,  $\langle 5d0|2p0 \rangle$ ; and  $\triangle$ ,  $\langle 5d1|2p1 \rangle$ ).

shows the calculated dependences of three kinds of overlap integrals on the distance between  $Ce^{3+}$  and  $F^-$  ions. For a convenience of application, they were approximated by polynomials of fourth order:  $S_t^{nl} = a_t + b_t R_L + c_t R_L^2 + d_t R_L^3 + e_t R_L^4$  ( $t = s, \sigma$ , or  $\pi$ ) for  $2.5 < R_L < 6$  a.u., and the fitting polynomial coefficients were listed in Table 3 with together two

**Table 3. Overlap Integrals of the 2s and 2p Wavefunctions of  $F^-$  Ion, Respectively, with the 5d Wavefunction of  $Ce^{3+}$  Ion and the 4f Wavefunction of  $Eu^{3+}$  Ion, and the Radial Moments of 5d Orbital of  $Ce^{3+}$  Ion and 4f Orbital of  $Eu^{3+}$  Ion**

	$Ce^{3+}(5d)^a$	$Eu^{3+}(4f)^a$
$a_s$	-0.6242	0.2712
$b_s$	1.3434	-0.0890
$c_s$	-0.5523	-0.0009
$d_s$	0.0859	0.0029
$e_s$	-0.0047	-0.0003
$a_\sigma$	2.6944	0.1298
$b_\sigma$	-2.3386	-0.2040
$c_\sigma$	0.6883	0.0795
$d_\sigma$	-0.0870	-0.0122
$e_\sigma$	0.0041	0.0007
$a_\pi$	0.9181	0.6033
$b_\pi$	-0.1300	-0.3968
$c_\pi$	-0.0713	0.1020
$d_\pi$	0.0191	-0.0120
$e_\pi$	-0.0012	0.0005
$\langle 5dlr^2 5d \rangle \text{\AA}^2$	1.5776	
$\langle 5dlr^4 5d \rangle \text{\AA}^4$	3.8604	
$\langle 4flr^2 4f \rangle \text{\AA}^2$		0.2321
$\langle 4flr^4 4f \rangle \text{\AA}^4$		0.1316
$\langle 4flr^6 4f \rangle \text{\AA}^6$		0.1603

<sup>a</sup>The overlap integrals  $S_t^{nl}(R_L)$  can be approximately written as a fourth order polynomial:  $a_t + b_t R_L + c_t R_L^2 + d_t R_L^3 + e_t R_L^4$ , where  $t = s, \sigma$ , or  $\pi$ ;  $nl = 4f$  or  $5d$ ; and  $2.5 < R_L < 6$  a.u.

moments of the 5d-electron density. Second, the similar steps were applied to  $\text{Eu}^{3+}$  ions except for making use of the analytical radial 4f wavefunctions of  $\text{Eu}^{3+}$  ions taken from ref 64 in the whole calculation process. The theoretical dependences of three kinds of overlap integrals on the distance between 4f electrons of  $\text{Eu}^{3+}$  and 2s and 2p electrons of  $\text{F}^-$  ions were plotted in Figure 4, and the corresponding fitting polynomial

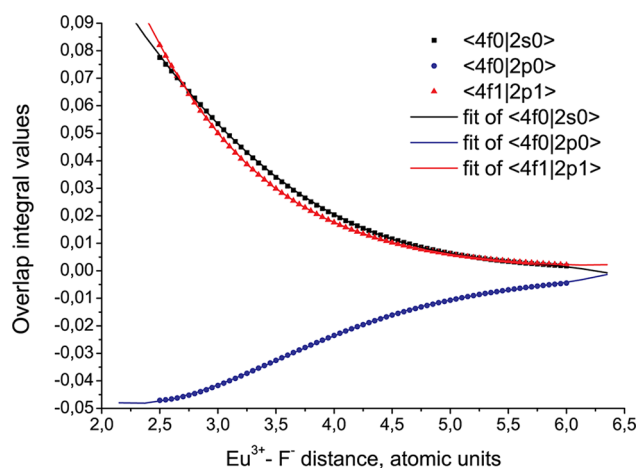


**Figure 4.** Calculated dependence of overlap integrals on the distance between  $\text{Eu}^{3+}$  and  $\text{F}^-$  ions ( $\square$ ,  $\langle 4f0|2s0 \rangle$ ;  $\circ$ ,  $\langle 4f0|2p0 \rangle$ ; and  $\triangle$ ,  $\langle 4f1|2p1 \rangle$ ).

coefficients and three moments of the 4f-electron density of  $\text{Eu}^{3+}$  ions were also collected in Table 3. Third, the *explicit* expressions of  $\beta_k$  for 5d electrons can be taken from ref 55, and those related values for 4f electrons can be derived from ref 65. Fourth, the ion charges  $q_i$  were fixed as  $-1$  ( $\text{F}^-$ ),  $+1$  ( $\text{K}^+$ ), and  $+3$  ( $\text{Y}^{3+}$ ). Finally, to ensure proper convergence of crystal lattice sums when calculating the contribution from point-charges of crystal lattice ions, three large clusters consisting of 35473 ions centered at the Y, K(1), and K(2) ions were generated by using the crystal structure data for  $\text{K}_3\text{YF}_6$  from ref 10; in this way, the ions located at the distances up to about 85 Å from the central  $\text{Ln}^{3+}$  ion were taken into account. Since the 5d CFPs of the  $\text{Ce}^{3+}$  ion can be obtained by fitting its 4f–5d excitation spectrum with the help of ECM, more details of the 5d CFP calculations of  $\text{Ce}^{3+}$  ion have been moved to section  $\text{Ce}^{3+}$ . In what follows, we concentrate on the introduction of the method to estimate the 4f CFPs using the ECM.

The determinations of three  $G$  parameters for  $\text{Eu}^{3+}$  ions in  $\text{K}_3\text{YF}_6$  are the key to calculating CFPs. According to the fact that the rationale of ECM shows that  $G$  parameters are only dependent on the properties of the ligand ions and the distance between the central  $\text{Ln}^{3+}$  ion and the ligand ions in general, the  $G$  parameter values for  $\text{Eu}^{3+}$  ions in the present host can be taken from those known values (extracted from the known CFPs or related f–f experimental spectral data) in some fluoride hosts with almost the same interionic coordination distance as  $\text{K}_3\text{YF}_6$ . The  $\text{Cs}_2\text{KYF}_6$  host is a good suitable candidate to be used to determine the present  $G$  parameters

**Table 4.** 4f CFP and CF Strength Values for  $\text{Eu}^{3+}$  Ions at the Y, K(1), and K(2) Sites of  $\text{K}_3\text{YF}_6$  and the Y Site of  $\text{Cs}_2\text{KYF}_6$  (unit,  $\text{cm}^{-1}$ )

	$\text{K}_3\text{YF}_6$									$\text{Cs}_2\text{KYF}_6$		
	Y site			K(1)			K(2)			Y site		
	$B_q^{(pc)k}$	$B_q^{(cc)k}$	total	$B_q^{(pc)k}$	$B_q^{(cc)k}$	total	$B_q^{(pc)k}$	$B_q^{(cc)k}$	total	$B_q^{(pc)k}$	$B_q^{(cc)k}$	total
$B_0^3(f)$	−41	−17	−58	−55	−9	−64	−139	−28	−167			
$B_1^3(f)^a$	6 + i18	14 + i33	20 + i51	21 − i57	−2 − i11	19 − i68	−11 − i94	3 − i3	−8 − i97			
$B_2^3(f)^a$	35 − i22	22 + i3	57 − i19	−31 − i98	−8 − i22	−39 − i120	−39 + i121	−4 + i19	−43 + i140			
$B_0^4(f)$	522	799	1321	236	167	403	8	−26	−18	1158	1835	2993
$B_1^4(f)^a$	−594 + i275	−966 + i440	−1560 + i715	202 − i68	142 − i53	344 − i121	−i4, 8 − i4	8 − i8				
$B_2^4(f)^a$	55 − i213	89 − i351	144 − i564	40 − i13	31 − i3	71 − i16	−27 + i78	−25 + i50	−52 + i128			
$B_3^4(f)^a$	−256 + i220	−416 + i333	−672 + i553	78 − i85	57 − i43	135 − i128	3 + i14	2 + i15	5 + i29			
$B_4^4(f)^a$	−377 + i462	−583 + i751	−960 + i1213	−164 + i155	−116 + i111	−280 + i266	−31 − i117	8 − i76	−23 − i193	692	1097	1789
$B_0^6(f)$	1	23	24	−3	1	−2	−15	−24	−39	65	363	428
$B_1^6(f)^a$	−8 + i31	−44 + i160	−52 + i191	4 − i9	16 − i27	20 − i36	−3 + i6	−13 + i19	−16 + i25			
$B_2^6(f)^a$	53 − i34	285 − i184	338 − i218	6 − i20	23 − i75	29 − i95	5 + i5	11 − i7	16 − i2			
$B_3^6(f)^a$	65 − i20	351 − i114	416 − i134	−16 + i4	−65 + i19	−81 + i23	5 + i4	21 + i17	26 + i21			
$B_4^6(f)^a$	16 − i37	116 − i205	132 − i242	5 − i13	46 − i52	50 − i65	−35	−75 − i2	−110 − i2	−122	−679	−801
$B_5^6(f)^a$	−21 + i75	−113 + i402	−134 + i477	11 − i14	39 − i53	50 − i57	−7	−23 + i10	−30 + i10			
$B_6^6(f)^a$	−10 − i55	−55 − i294	−65 − i349	7 − i6	30 − i13	37 − i19	3 − i3	12 − i26	15 − i29			
$N_2(B^2(f))^b$			203			340			475			
$N_4(B^4(f))^b$			4517			1060			401			4631
$N_6(B^6(f))^b$			1275			257			181			1190
$N_6(f)^b$			4698			1143			648			4781

<sup>a</sup>The CFPs for  $q < 0$  are related to ones for  $q > 0$  by  $B_{-q}^k(f) = (-1)^q B_q^{k*}(f)$ . <sup>b</sup> $N_2(B^2(f))$ ,  $N_4(B^4(f))$ ,  $N_6(B^6(f))$ , and  $N_6(f)$  are, respectively, the second, fourth, and sixth rank, and total CF strength parameters, defined by Auzel et al.<sup>38</sup>



because its Y–F interionic distance of  $2.156 \text{ \AA}^{13}$  is very similar to that in  $\text{K}_3\text{YF}_6$  (about  $2.16 \text{ \AA}^{10}$ ), and CFP values of  $\text{Eu}^{3+}$  ions in this host have been provided in ref 66, which makes the extraction of  $G$  parameters possible. In addition, the doped site in this host has very high symmetry  $O_h$  so that only two independent CFPs  $B_0^4(f)$  and  $B_0^6(f)$ <sup>67</sup> need to be considered, which greatly simplifies the ECM calculations. Nevertheless, this also means only two fitting parameters can be introduced into the whole fitting. Thus, we assumed the values of  $G_s$  and  $G_\sigma$  for  $4f$  electron to be the same (i.e.,  $G_s = G_\sigma = G_{s\sigma}$ ) as previously supposed by refs 51, 52, and 54. Before fitting  $G_{s\sigma}$  and  $G_\pi$  parameters, a large cluster including 43 721 ions with a  $\text{Y}^{3+}$  (replaced by a  $\text{Ln}^{3+}$ ) ion at the center was obtained to ensure the proper convergence of crystal lattice sums by using the crystal structure data for  $\text{Cs}_2\text{KYF}_6$  from ref 13, and the ion charges  $q_i$  were fixed as  $-1$  ( $\text{F}^-$ ),  $+1$  ( $\text{K}^+$  and  $\text{Cs}^+$ ), and  $+3$  ( $\text{Y}^{3+}$ ). After using the structure information of this cluster and substituting various parameter values listed in Table 3 into eqs 6 and 7, we obtain the two  $G$  parameter values (i.e.,  $G_{s\sigma} = 4.15$  and  $G_\pi = 2.95$ ) by fitting the calculated  $4f$  CFP values for  $\text{Eu}^{3+}$  ions doped in  $\text{Cs}_2\text{KYF}_6$  host given by ref 66. The similarity with  $G$  parameter values for  $4f$  CFP of  $\text{Ho}^{3+}$  ions in  $\text{LiYF}_4$  reported in ref 51 confirms the rationality and validity of the present fitting. On the basis of these agreements and the above ideas, we believe that the reliable obtained  $G$  parameters from  $\text{Eu}^{3+}$  ions doped in the  $\text{Cs}_2\text{KYF}_6$  host can be further applied to the  $\text{K}_3\text{YF}_6$  host. Three sets of  $4f$  CFPs of  $\text{Eu}^{3+}$  ions in  $\text{K}_3\text{YF}_6$  host for three different sites (Y, K(1), and K(2)) were calculated by repeatedly employing eqs 6 and 7, various parameter values in Table 3, and the cluster structure information of every possible site, and they were also collected in Table 4 with  $4f$  CFPs of  $\text{Eu}^{3+}$  ions doped in the  $\text{Cs}_2\text{KYF}_6$  host together.

Since the CF strength parameter can be used to well character the magnitude of the maximum Stark splitting of one  $J$ -manifold for ions in crystals of different structures and site symmetries,<sup>38,68</sup> we had evaluated the CF strength parameters for every set of CFPs and also listed them in Table 4. It is seen from Table 4 that the calculated CFP and corresponding CF strength values for the Y site are much larger than those for two K sites. This is due to the relatively shorter coordination distance of the Y site than the another two sites.

**Other Competitive Excitation Channels in the High-Energy Spectral Region. Host Absorption.** The host absorption obscuring the high energy parts of electronic structure of  $4f^{N-1}5d$  configuration of  $\text{Ln}^{3+}$  ions is the most commonly observed in the excitation spectra of  $\text{Ln}^{3+}$  ions in host. The absorption energy of the host lattice can be obtained by measuring the optical properties of the undoped sample and further confirmed in the excitation spectra of different  $\text{Ln}^{3+}$  ions in the same host lattices due to the intrinsic property of the band-to-band transition. Figure 5 shows the optical excitation spectrum of the pure  $\text{K}_3\text{YF}_6$  crystal of the self-trapped exciton (STE) emission with a wavelength of  $450 \text{ nm}$  at  $10 \text{ K}$ . The first excitation band around  $91\,700 \text{ cm}^{-1}$  ( $E_{\text{ex}}$ ) is attributed to the exciton creation peak of the host lattice. From the onset of the low energy side of this peak, the threshold for the fundamental absorption of the host lattice  $E_{\text{fa}}$  can be taken as  $86\,500 \text{ cm}^{-1}$ . Following the assignment of the exciton peak, the band gap between the valence and conduction bands  $E_{\text{vc}}$  can be estimated as  $100\,000 \text{ cm}^{-1}$ , which basically agrees with the threshold of the next excitation peak. The present assignment coincides fairly well with the observed values (about  $90\,000 \text{ cm}^{-1}$ ) of host excitation in the excitation spectra of  $\text{Ce}^{3+}$ ,  $\text{Pr}^{3+}$ ,  $\text{Eu}^{3+}$ ,  $\text{Gd}^{3+}$ , and

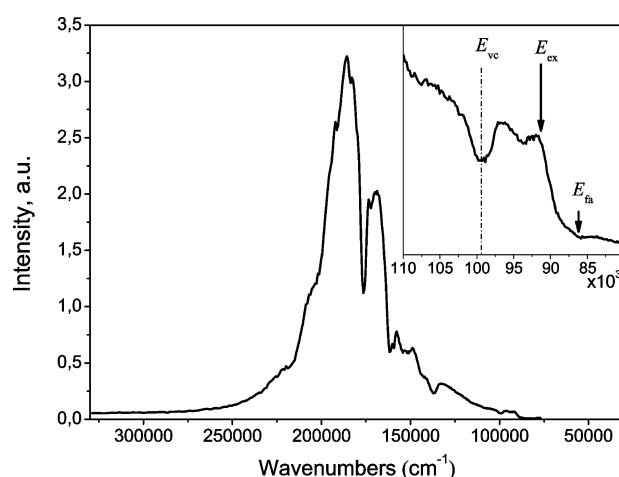


**Figure 5.** Optical excitation spectrum of a pure  $\text{K}_3\text{YF}_6$  crystal of the self-trapped exciton emission at a wavelength of  $450 \text{ nm}$  at  $10 \text{ K}$ . The inset figure shows the fine structures around the onset region of the excitation spectrum.

$\text{Er}^{3+}$  ions doped in  $\text{K}_3\text{YF}_6$  (see Figures 8, 9, 11, 12, and 15). Other features of host excitation at photon energies bigger than  $100\,000 \text{ cm}^{-1}$  are also shown, but these bands are not usually paid close attention to due to much lower efficient energy transfer to luminescent impurity centers after their excitation.

**Charge Transfer (CT) Transition.** The CT transitions of  $\text{Ln}^{3+}$  ions in about 200 different compounds have been collected and systematically reanalyzed by Dorenbos.<sup>26,27</sup> Meanwhile, one simple formula to predict the CT transition energy of  $\text{Ln}^{3+}$  ions in host has also been proposed by him based on the empirical regularity summarized from a large number of experimental data:

$$E_{\text{CT}}(\text{Ln}^{3+}) = E_{\text{CT}}(\text{Eu}^{3+}) + \Delta E_{\text{CT}}(\text{Ln}^{3+}, \text{Eu}^{3+}) \quad (9)$$

where the first term represents the observed CT transition energy of  $\text{Eu}^{3+}$  ion in the same lattice site, and the last term is the difference between the CT energies of  $\text{Ln}^{3+}$  and  $\text{Eu}^{3+}$  ions and assumed as a host independent constant given in ref 27. The inevitable relaxation involved in the CT transition process generally leads to large Stokes shift and broad absorption or emission bands to appear,<sup>69</sup> which means the threshold and maximum of CT transition bands both need to be considered and determined. In this work, the Stokes shifts and fwhm of CT transition bands for all  $\text{Ln}^{3+}$  ions in the same crystal lattice are assumed to be the same, which is similar to the descriptions of  $4f$ – $5d$  transition broad bands. Thus, now eq 9 without any modification can be applied to the estimations of the threshold ( $E_{\text{CT}}(\text{Ln}^{3+}, \text{onset})$ ) and maximum ( $E_{\text{CT}}(\text{Ln}^{3+}, \text{max})$ ) values of the CT transition band of any  $\text{Ln}^{3+}$  ion in  $\text{K}_3\text{YF}_6$  by means of referring to those values of  $\text{Eu}^{3+}$  ion in  $\text{K}_3\text{YF}_6$  where  $E_{\text{CT}}(\text{Eu}^{3+}, \text{onset}) \approx 55\,600 \text{ cm}^{-1}$  and  $E_{\text{CT}}(\text{Eu}^{3+}, \text{max}) \approx 63\,700 \text{ cm}^{-1}$  (see Figure 11). The measured and calculated values of CT transition energies for  $\text{Ln}^{3+}$  ions in  $\text{K}_3\text{YF}_6$  have been collected in Table 5. These values seem to be shifted to short wavelength direction by about  $3500 \text{ cm}^{-1}$  relative to those in similar elpasolite system  $\text{Cs}_2\text{NaYF}_6$  doped with  $\text{Ln}^{3+}$  ions.<sup>9</sup>

**4f–4f Transition.** There maybe be some energy overlaps between the  $4f$ – $4f$  and  $4f$ – $5d$  transitions in the VUV region.<sup>71</sup> The former is formally parity-forbidden, which results in much weaker transition intensities than the parity-allowed later. Therefore, the  $4f$ – $4f$  transitions are not observed and always

**Table 5.** Calculated and Measured Threshold and Maximum Energy Values of CT Transition Bands ( $E_{\text{CT}}(Ln^{3+}, \text{onset})$  and  $E_{\text{CT}}(Ln^{3+}, \text{max})$ ), and Maximum Energy Values of the Lowest 4f–5d and 4f–6s Transition Bands ( $E_{\text{fd}}(Ln^{3+})$  and  $E_{\text{fs}}(Ln^{3+})$ ) for  $Ln^{3+}$  Ions in  $K_3YF_6$ <sup>a</sup>

$Ln^{3+}$	$\Delta E_{\text{CT}}(Ln^{3+}, Eu^{3+})^c$		$E_{\text{CT}}(Ln^{3+}, \text{onset})$		$E_{\text{CT}}(Ln^{3+}, \text{max})$		$\Delta E_{\text{fd}}(Ln^{3+}, Ce^{3+})^{b,c}$		$E_{\text{fd}}(Ln^{3+})^b$		$\Delta E_{\text{fs}}(Ln^{3+}, Ce^{3+})^b$		$E_{\text{fs}}(Ln^{3+})^b$	
	calcd (or emp.)		calcd	exptl <sup>d</sup>	calcd	exptl <sup>d</sup>	calcd (or emp.)		calcd	exptl <sup>d</sup>	calcd		calcd	exptl <sup>d</sup>
Ce <sup>3+</sup>	31.2		86.8		94.9		0		34.3	34.3	0		70.0	70.0
Pr <sup>3+</sup>	19.7		75.3	75.8	83.4	79.4	12.2		46.5	45.6	12.8		82.8	
Nd <sup>3+</sup>	18.5		74.1		82.2		22.7		57.0	56.8	23.2		93.2	
Pm <sup>3+</sup>	18.1		73.7		81.8		25.7		60.0		26.3		96.3	
Sm <sup>3+</sup>	9.4		65.0		73.1		26.5		60.8		27.8		97.8	
Eu <sup>3+</sup>	0		55.6	55.6	63.7	63.7	35.9		70.2	67.9	36.2		106.2	
Gd <sup>3+</sup>	34.8		90.4		98.5		45.8		80.1	78.4	44.6		114.6	
Tb <sup>3+</sup>	25.2		80.8		88.9		13.2(5.4)		47.5(39.7)	47.1 (38.2)	5.9 (1.5)		75.9 (71.5)	76.2
Dy <sup>3+</sup>	16.5		72.1		80.2		25.1(17.7)		59.4(52.0)	59.4 (50.4)	13.2 (9.7)		83.2 (79.7)	
Ho <sup>3+</sup>	19.5		75.1		83.2		31.8(29.1)		66.1(63.4)		18.3 (15.4)		88.3 (85.4)	
Er <sup>3+</sup>	18.2		73.8		81.9		30.0(27.0)		64.3(61.3)	65.1 (61.4)	13.6 (11.3)		83.6 (81.3)	
Tm <sup>3+</sup>	13.5		69.1		77.2		29.3(27.0)		63.6(61.3)		8.5 (6.8)		78.5 (76.8)	
Yb <sup>3+</sup>	3.5		59.1		67.2		38.0(36.4)*		72.3(70.7)*		13.7 (12.5)		83.7 (82.5)	
Lu <sup>3+</sup>							49.2(48.3)*		83.5(82.6)*		20.1 (19.5)		90.1 (89.5)	

<sup>a</sup>More details of the definitions of various symbols and the related phenomenological models can be found in the text (unit,  $10^3 \text{ cm}^{-1}$ ). <sup>b</sup>The data in the parentheses represent the lowest 4f–5d or 4f–6s SF transition energies of heavy  $Ln^{3+}$  ions. The data marked with the asterisks are obtained by using the extended simple model proposed by Duan and Reid et al.<sup>70</sup> <sup>c</sup>The data for  $\Delta E_{\text{CT}}(Ln^{3+}; Eu^{3+})$  and  $\Delta E_{\text{fd}}(Ln^{3+}; Ce^{3+})$  are, respectively, taken from refs 27, and 24 and 25. <sup>d</sup>The measured data of the Y site were used because the lower energy experimental data for the K(1) site are always buried in the transition broad bands belonging to the Y site so that they are not distinguished very well.

buried by intense 4f–5d transitions with broad band structures occurring in the same energy region, as ref 71 described. However, for some heavy  $Ln^{3+}$  ions, very weak spin-forbidden (SF) 4f–5d transitions<sup>72</sup> may provide the existent space for 4f–4f transitions. For instance, in the excitation spectrum of  $Dy^{3+}$  ions doped in  $LiYF_4$ , some sharp lines situated between two weak HS states of  $4f^85d$  configuration around 192 and 182 nm may be due to intraconfigurational 4f<sup>9</sup> transition.<sup>21,73</sup> For our present host, this case was not found.

**4f–6s Transition.** Another possible competitive excitation channel sometimes forgotten is the 4f–6s transition. It is ostensibly electric-dipole forbidden because the absolute value of the change in orbital quantum number  $l$  of the outmost excited electron is not equal to 1 (i.e.,  $\Delta l = f - s \neq 1$ ). However, the failed selection rule can be relifted by combining the mixing between  $4f^{N-1}6s$  and  $4f^{N-1}5d$  configurations due to the Coulomb and CF interactions between these two configurations. This means that the 4f–6s transition is not much weaker and may be separated from the 4f–5d excitation spectra of  $Ln^{3+}$  ions in host. In the following, we proposed a theoretical scheme to consider the 4f–6s transition of  $Ln^{3+}$  ion in host.

According to the effective Hamiltonian theory,<sup>74</sup> the effective Hamiltonian for  $4f^{N-1}6s$  configurations of lanthanide ions in crystals can be expressed as

$$\mathcal{H}(4f^{N-1}6s) = \mathcal{H}(\text{ff}) + \mathcal{H}_{\text{coul}}(\text{fs}) + \Delta_E(\text{fs}) + \mathcal{H}_{\text{Cl}}(\text{ds}) \quad (10)$$

where the meanings of first three terms are very similar to those in the  $4f^{N-1}5d$  configuration, the last term shows the correction of configuration interactions between  $4f^{N-1}5d$  and  $4f^{N-1}6s$  configurations, and the CF and spin–orbit interactions for single 6s electron do not have any contribution to configurational energy splitting due to the spherically symmetrical s orbital. For  $\mathcal{H}_{\text{coul}}(\text{fs})$ , there only appears the exchange part with third rank due to the selection rule between orbital quantum

numbers of 4f and 6s electrons. Following the theory of an effective exchange Coulomb operator proposed by Cowan (i.e., equation (11.93) of ref 75),  $\mathcal{H}_{\text{coul}}(\text{fs})$  due to the quenching of the orbital operator of the 6s electron can be further written as follows:

$$\mathcal{H}_{\text{coul}}(\text{fs}) = -\frac{2}{7}G^3(\text{fs})S_f s_s \quad (11)$$

where  $S_f$  and  $s_s$  are, respectively, the total spin operator of  $N - 1$  4f electrons and the spin operator of single 6s electron, and  $G^3(\text{fs})$  is the Slater integral of 4f–6s exchange Coulomb interaction. For  $\mathcal{H}_{\text{Cl}}(\text{ds})$ , in terms of the perturbation theory<sup>76</sup> and the closure approximation made by Judd or Ofelt,<sup>77,78</sup> it can be approximately expressed as

$$\mathcal{H}_{\text{Cl}} = \sum_{\Psi} \frac{(\mathcal{H}_{\text{cf}}(\text{ds}) + \mathcal{H}_{\text{coul}}(\text{ds}))|\Psi\rangle\langle\Psi|(\mathcal{H}_{\text{cf}}(\text{ds}) + \mathcal{H}_{\text{coul}}(\text{ds}))}{\Delta_E(\text{fs}) - \Delta_E(\text{fd})} \quad (12)$$

where  $\mathcal{H}_{\text{cf}}(\text{ds})$  and  $\mathcal{H}_{\text{coul}}(\text{ds})$  are, respectively, the CF and Coulomb interactions between 5d and 6s electrons, and  $\Psi$  stands for any possible state of  $4f^{N-1}5d$  configuration. By inspecting eq 12 and considering its selection rules of energy matrix elements within  $4f^{N-1}6s$  configuration, one can find only the following parameters: two 5d–6s Coulomb Slater integrals (direct one  $F^2(4f6s, 4f5d)$  and exchange one  $G^3(6s4f, 4f5d)$ ) and CFPs between 5d and 6s electrons with  $k = 2(B_q^2(\text{ds})$ , for which the possible value of  $q$  is dependent on the site symmetry). Moreover,  $B_q^2(\text{ds})$  is proportional to the expectation values of the  $r^2$  between 5d and 6s orbitals ( $\langle 5d||r^2||6s \rangle$ ) and can be roughly estimated by using the point-charge calculation of ECM since the dominant contribution for  $B_q^2(\text{ds})$  is from long-range electrostatic interactions.<sup>59</sup> The complete parametrized calculation is very similar to that for the  $4f^{N-1}5d$  configuration. However, very few observed data and the spectral character

with broad vibronic bands greatly restrict the possible parameter fitting scheme. Therefore, a good estimate of parameters would be needed. The values of  $\Delta_E(\text{fs})$ ,  $F^k(\text{ff})$  ( $k = 2, 4, 6$ ),  $\zeta_f(\text{f})$ ,  $G^3(\text{fs})$ ,  $F^2(4f6s, 4f5d)$ ,  $G^3(6s4f, 4f5d)$ ,  $\langle 4f|r^k|4f \rangle$  ( $k = 2, 4, 6$ ) and  $\langle 5d|r^2|6s \rangle$  for ions across the lanthanide series were calculated by using the standard atomic-physics codes of Cowan<sup>75</sup> and listed in Table 6.

It is seen from Table 6 that the direct and exchange 5d–6s Coulomb Slater integrals are, respectively, about 3300 and 6700  $\text{cm}^{-1}$  and will become even smaller if considering the nephelauxetic effect, which strongly suggests that the contribution imposed by 5d–6s Coulomb interaction can be ignored due to a very large energy difference between the barycenters of the two configurations  $4f^N5d$  and  $4f^{N-1}6s$  ( $\sim 20\,000\text{ cm}^{-1}$  deduced from Table 6). The calculated  $B_q^2(\text{ds})$  can be taken as the value of the corresponding second rank 5d CFPs multiplied by the ratio  $\langle 5d|r^2|6s \rangle / \langle 5d|r^2|5d \rangle$ . A direct estimation of magnitude order of the contribution of the CF part of  $\mathcal{H}_{\text{CI}}(\text{ds})$  will be crucial to understanding the configuration interaction rather than very complicated calculation without any approximation. The derivation process of the matrix elements of the CF part of  $\mathcal{H}_{\text{CI}}(\text{ds})$  between the standard JM bases of the  $4f^{N-1}6s$  configuration looks almost the same as that of the Judd–Ofelt theory<sup>77,78</sup> due to both adopting the closure approximation, and two  $\mathcal{H}_{\text{CI}}(\text{ds})$  operators in the numerator of eq 12 will be united into a single operator that acts between states of the  $4f^{N-1}6s$  configuration. Therefore, the ratio of the second rank CF strength between 5d and 6s electrons,  $N_v^2(\text{ds})$  to energy difference between the barycenters of the two configurations  $4f^N5d$  and  $4f^{N-1}6s$  (estimated as  $\sim 20\,000\text{ cm}^{-1}$  from Table 6), can be used to simply evaluate the magnitude order of the contribution of the CF part of  $\mathcal{H}_{\text{CI}}(\text{ds})$ . One can also conclude the fact that  $N_v^2(\text{ds})$  is about 65.3 times larger than  $N_v^2(\text{f})$  by calculating the square of the ratio of  $\langle 5d|r^2|6s \rangle$  to  $\langle 4f|r^2|4f \rangle$  after referring to Tables 3 and 6. In addition, the maximum Stark splitting of one  $J$ -manifold for  $\text{Ln}^{3+}$  ions in host is proportional to the CF strength, and the magnitude order of the maximum CF splitting is about  $10^2\text{ cm}^{-1}$ ,<sup>38</sup> as we all know. On the basis of the above facts, the magnitude order of the contribution of the CF part of  $\mathcal{H}_{\text{CI}}(\text{ds})$  can be estimated as  $10^2\text{ cm}^{-1}$ , which is very small and means the CF effect of  $\mathcal{H}_{\text{CI}}(\text{ds})$  can be fully neglected in nature.

If  $\mathcal{H}_{\text{CI}}(\text{ds})$  and the CF potential in the  $\mathcal{H}(\text{ff})$  are both ignored because the energy splittings caused by them are of the same order of magnitude as optical phonon energies and sometimes cannot be well-resolved experimentally,  $\mathcal{H}(4f^{N-1}6s)$  will commute with the total angular momentum operator  $J = S_f + s_s + L_f + l_s$  where the subscripts f and s are used to show that the operators act on  $N - 1$  4f and single 6s electrons, respectively. For the  $4f^{N-1}6s$  configuration, the spin–orbit coupling interaction of the 4f electrons is always stronger than the exchange 4f–6s Coulomb interaction due to the smaller exchange Coulomb integral  $G^3(\text{fs})$  as shown in the Table 6. In the case of  $\text{Pr}^{3+}$  ions, the magnitude order of energy splitting induced by the exchange 4f–6s Coulomb interaction is about  $1100\text{ cm}^{-1}$ , which is weaker than the well-known spin–orbit splitting of  $4f^1$  core ( $\sim 2000\text{ cm}^{-1}$ ). Therefore, the coupling scheme ( $((\text{SO}_3^S \times \text{SO}_3^L)_f \times \text{SO}_3^S)_f \times \text{SO}_3^S)_f$ ) may be preferred, and the approximate eigen-energies can be written as

Table 6. Calculated Parameters and Radial Integrals for the  $4f^{N-1}6s$  Configuration of  $\text{Ln}^{3+}$  Ions<sup>a</sup>

$\text{Ln}^{3+}$	$\text{Ce}^{3+}$	$\text{Pr}^{3+}$	$\text{Nd}^{3+}$	$\text{Pm}^{3+}$	$\text{Sm}^{3+}$	$\text{Eu}^{3+}$	$\text{Gd}^{3+}$	$\text{Tb}^{3+}$	$\text{Dy}^{3+}$	$\text{Ho}^{3+}$	$\text{Er}^{3+}$	$\text{Tm}^{3+}$	$\text{Yb}^{3+}$	$\text{Lu}^{3+}$
$\Delta_E(\text{fd, free ion})^b$	57812	65413	71773	77635	82813	87401	91584	95256	98526	101535	104024	106306	108203	109809
$\Delta_E(\text{fs, Cs}_2\text{NaYCl}_6)$	65907	70682	74585	78123	80671	82951	83815	84487	85138	85748	86227	86631	87542	[85033] <sup>c</sup>
$\Delta_E(\text{fs, free ion})$	89862	96871	102589	107416	111547	114984	117758	120047	121750	123009	123901	124226	124253	123950
$F^2(\text{ff})$			108981	112436	115780	119028	122188	125285	128314	131289	134221	137100	139944	
$F^4(\text{ff})$			68669	70830	72919	74944	76911	78837	80718	82563	84381	86163	87924	
$F^6(\text{ff})$			49483	51036	52536	53989	55400	56780	58128	59449	60751	62026	63286	
$\zeta_f(\text{f})$		908	1041	1185	1340	1507	1687	1880	2087	2309	2547	2801	3071	3359
$G^3(\text{fs})$		3859	3849	3830	3814	3803	3795	3789	3787	3787	3788	3792	3797	3803
$F^2(4f6s, 4f5d)$		2546	2727	2958	3142	3266	3336	3378	3367	3334	3284	3174	3059	2935
$G^3(6s4f, 4f5d)$		6520	6573	6658	6724	6768	6794	6810	6808	6799	6783	6748	6711	6671
$\langle 4f r^2 4f \rangle$		0.2909	0.2755	0.2593	0.2449	0.2321	0.2206	0.2101	0.2006	0.1919	0.1839	0.1765	0.1697	0.1634
$\langle 4f r^4 4f \rangle$		0.1805	0.1643	0.1468	0.1321	0.1197	0.1091	0.1000	0.0920	0.0850	0.0788	0.0733	0.0684	0.0640
$\langle 4f r^6 4f \rangle$		0.2055	0.1820	0.1556	0.1346	0.1176	0.1037	0.0921	0.0823	0.0741	0.0670	0.0609	0.0556	0.0510
$\langle 5d r^2 6s \rangle$	−1.8760	−1.8295	−1.7870	−1.7496	−1.7156	−1.6846	−1.6563	−1.6301	−1.6059	−1.5834	−1.5622	−1.5425	−1.5239	−1.5063

<sup>a</sup>Parameters have units  $\text{cm}^{-1}$  and radial integrals have units  $\text{\AA}^k$ . The definitions of various symbols have been provided in the text. <sup>b</sup>The values of  $\Delta E(\text{fd, free ion})$  were taken from Table 1 in ref 42. <sup>c</sup>The value in square brackets is extrapolated from the trend of the parameter  $\Delta E(\text{fs, Cs}_2\text{NaYCl}_6)$  for the whole lanthanide series.



$$\begin{aligned}
 & E(|[(4f^{N-1}\eta_f S_f L_f J_f, s_f)J, l_s]J\rangle) \\
 &= \Delta_E(\text{fs}) + E(4f^{N-1}\eta_f S_f L_f J_f) - G^3(\text{fs}) \\
 & \quad \frac{J_f(J_f + 1) + S_f(S_f + 1) - L_f(L_f + 1)}{14J_f(J_f + 1)} \\
 & \quad \times \left[ J(J + 1) - J_f(J_f + 1) - \frac{3}{4} \right] \quad (13)
 \end{aligned}$$

where the second term represents the splitting energy of the spin–orbit coupling interaction of the  $4f^{N-1}$  core (i.e., the energy difference between  $4f^{N-1}\eta_f S_f L_f J_f$  energy level and barycenter of the  $4f^{N-1}$  core), and the derivation of the last term is similar to eq 10 in ref 70.

The lower 4f–6s transition energy of  $Ln^{3+}$  in host is very interesting for all and can be easily obtained by using the following equation:

$$\begin{aligned}
 E_{fs}(Ln^{3+}) &= E_{\text{avg}}(N) + \Delta_E(\text{fs}) - E_{\text{avg}}(N - 1) \\
 & - G^3(\text{fs}) \frac{J_f(J_f + 1) + S_f(S_f + 1) - L_f(L_f + 1)}{14J_f(J_f + 1)} \\
 & \times \left[ J(J + 1) - J_f(J_f + 1) - \frac{3}{4} \right] \quad (14)
 \end{aligned}$$

where  $S_f$ ,  $L_f$ , and  $J_f$  are the angular momentum quantum numbers of the lowest energy level of the  $4f^{N-1}$  core and  $J = J_f + 1/2$  or  $J_f - 1/2$  (transitions to the two  $J$  quantum states from the  $4f^N$  ground states are, respectively, SF and spin-allowed (SA) for last half series, whereas it is contrary for first last series);  $E_{\text{avg}}$  is the energy separation between the energies of the lowest level of the  $4f^N$  and barycenter of the  $4f^N$  configuration and can be approximately taken from the values listed in Table 2 due to the small splittings caused by the 4f CF interaction. It is noted that the calculated values of  $\Delta_E(\text{fs})$  for free ions listed in Table 6 can not be applied to the case of host due to the bigger suppression of the  $4f^{N-1}6s$  configuration centroid imposed by CF environment.<sup>79</sup> To determine the values of  $\Delta_E(\text{fs})$  of  $Ln^{3+}$  ions in  $K_3YF_6$  host, we assumed the dependence of  $\Delta_E(\text{fs})$  upon  $N$  to be independent of the host although  $\Delta_E(\text{fs})$  itself is strongly correlated to hosts. This assumption can be further checked by the ab initio calculations of some systems doped with  $Ln^{3+}$  ions. Our previous ab initio calculations of electronic structures of  $Cs_2NaYCl_6:Ln^{3+80}$  gave the transition energy values from the highest occupied 4f molecular orbital (MO) to 6s orbital for ions across lanthanide series. By using the CF energy level calculations of single 4f electron with the 4f spin–orbit parameter and CFPs of every ion listed in ref 37 to simply the energy difference between the 4f highest occupied molecular orbital and barycenter of all the MOs into account, the  $\Delta_E(\text{fs})$  values of ions across lanthanide series in  $Cs_2NaYCl_6$  were obtained and listed in Table 6, and the related variation trend with  $N$  increasing was also plotted in the Figure 6 with that for free ions together. It is seen from Figure 6 that the dependence of  $\Delta_E(\text{fs})$  of free ions is very similar to that of  $Ln^{3+}$  in  $Cs_2NaYCl_6$ , respectively, upon light or heavy lanthanide series. As a rough estimation, the present assumption is relatively rational. Thus, the first 4f–6s transition energy of any ion in  $K_3YF_6$  host can be calculated by means of that of  $Ce^{3+}$  ions, the dependence of  $\Delta_E(\text{fs})$  upon  $N$  and eq 14. According to this idea, eq 14 can be further simplified as follows:

$$E_{fs}(Ln^{3+}) = E_{fs}(Ce^{3+}) + \Delta E_{fs}(Ln^{3+}, Ce^{3+}) \quad (15)$$

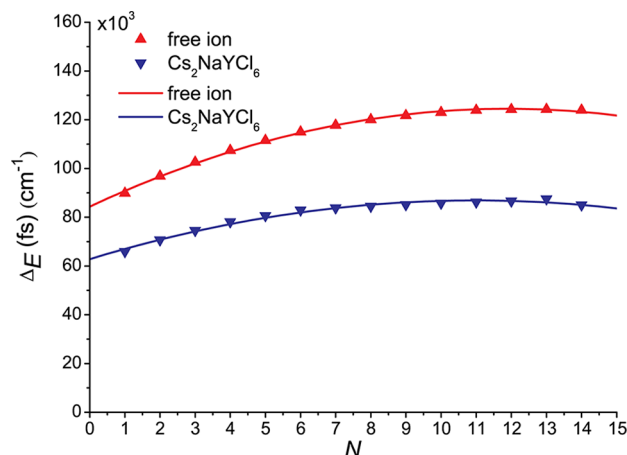


**Figure 6.** Dependence of the energy difference between the barycenters of  $4f^N$  and  $4f^{N-1}6s$  configurations  $\Delta_E(\text{fs})$  upon the electron number  $N$ . The fitting curves with a second-order polynomial for two cases (free ions and  $Ln^{3+}$  ions in  $Cs_2NaYCl_6$  host) are, respectively, written as  $84369 + 6758N - 284N^2$  and  $62826 + 4393N - 200N^2$  (unit,  $\text{cm}^{-1}$ ).

where

$$\begin{aligned}
 \Delta E_{fs}(Ln^{3+}, Ce^{3+}) &= (E_{\text{avg}}(N) - E_{\text{avg}}(1)) \\
 & + [\Delta_E(\text{fs}, N) - \Delta_E(\text{fs}, 1)] - E_{\text{avg}}(N - 1) \\
 & - G^3(\text{fs}) \frac{J_f(J_f + 1) + S_f(S_f + 1) - L_f(L_f + 1)}{14J_f(J_f + 1)} \\
 & \times \left[ J(J + 1) - J_f(J_f + 1) - \frac{3}{4} \right] \quad (16)
 \end{aligned}$$

The values of the second term (i.e.,  $[\Delta_E(\text{fs}, N) - \Delta_E(\text{fs}, 1)]$ ) in eq 16 will be averaged over two cases (free ion and  $Cs_2NaYCl_6$  host) for which data are available in Table 6.  $\Delta E_{fs}(Ln^{3+}, Ce^{3+})$  can be calculated by applying eq 16 and are collected in the Table 5 for reference.  $E_{fs}(Ln^{3+})$  in  $K_3YF_6$  can be simply determined by making use of eq 15, the fixed  $\Delta E_{fs}(Ln^{3+}, Ce^{3+})$  values and the fact that the first 4f–6s transition energy of  $Ce^{3+}$  ions in  $K_3YF_6$  ( $E_{fs}(Ce^{3+})$ ) is located at  $70\,000\text{ cm}^{-1}$  (see Figure 8). The measured and calculated values of  $E_{fs}(Ln^{3+})$  for  $Ln^{3+}$  ions in  $K_3YF_6$  were collected in Table 5.

#### $Ln^{3+}$ Energy Levels and Band Structure Gap of $K_3YF_6$ Host.

An intuitive understanding of various transitions appearing in the excitation spectra of  $Ln^{3+}$  ions doped in  $K_3YF_6$  is to label out the lowest energy level positions for  $4f^N$ ,  $4f^{N+1}(np)^5$  (where the symbol denotes CT states and np is the outermost orbital of  $F^-$  ligand ions),  $4f^{N-1}5d$ , and  $4f^{N-1}6s$  configurations in the band gap. For the CT transitions, it is very easy to determine the energy positions of the initial and final states (i.e., the top of the valence band and  $4f^{N+1}(np)^5$ , between which the transition energies can be found in Table 5. The energy positions of the final states of CT transitions of  $Ln^{3+}$  ions  $E_{VCT}(Ln^{3+})$  were listed in Table 7. For the lowest 4f–5d absorption, the complete calculation using the software packages can give its accurate transition energy, but here, we use the simplified formula given by Dorenbos<sup>24</sup> due to the approximate character of our diagram only for showing a physics understanding. This approximated equation is expressed as



Table 7. Lowest Energy Level Positions of  $4f^N$ ,  $4f^{N+1}(np)^5$ ,  $4f^{N-1}5d$ , and  $4f^{N-1}6s$  Configurations Relative to the Top of Valence Band ( $E_{VF}(Ln^{3+})$ ,  $E_{VCT}(Ln^{3+})$ ,  $E_{VD}(Ln^{3+})$ , and  $E_{VS}(Ln^{3+})$ ); Units are  $10^3 \text{ cm}^{-1}$

$Ln^{3+}$	$Ce^{3+}$	$Pr^{3+}$	$Nd^{3+}$	$Pm^{3+}$	$Sm^{3+}$	$Eu^{3+}$	$Gd^{3+}$	$Tb^{3+}$	$Dy^{3+}$	$Ho^{3+}$	$Er^{3+}$	$Tm^{3+}$	$Yb^{3+}$	$Lu^{3+}$
$E_{VF}(Ln^{3+}, Ce^{3+})$	0	-12.5	-23.1	-26.3	-26.9	-35.8	-46.2	-6.7	-18.2	-26.2	-24.4	-23.6	-32.7	-43.2
$E_{VF}(Ln^{3+})$	52.0	39.5	28.9	25.7	25.1	16.2	5.8	45.3	33.8	25.8	27.6	28.4	19.3	8.8
$E_{VCT}(Ln^{3+})$	86.8	75.3	74.1	73.7	65.0	55.6	90.4	80.8	72.1	75.1	73.8	69.1	59.1	
$E_{VD}(Ln^{3+})^a$	86.3	85.9	85.9	85.7	85.9	86.4	85.9	92.8 (85.0)	93.2 (85.8)	91.9 (89.2)	91.9 (88.9)	92.0 (89.7)	91.6 (90.0)	92.3 (91.4)
$E_{VS}(Ln^{3+})^a$	122.0	122.2	122.1	122.0	122.9	122.4	120.4	121.2 (116.8)	117.0 (113.5)	114.1 (111.2)	111.2 (108.9)	106.9 (105.2)	103.0 (101.8)	98.9 (98.3)

<sup>a</sup>The data in the parentheses represent the energy positions of the lowest 5d and 6s HS states for heavy  $Ln^{3+}$  ions in the band gap.

$$E_{fd}(Ln^{3+}) = E_{fd}(Ce^{3+}) + \Delta E_{fd}(Ln^{3+}, Ce^{3+}) \quad (17)$$

where the first term represents the first observed 4f–5d transition energy of  $Ce^{3+}$  ion in the same lattice site, and the last term is the difference between the first 4f–5d transition energies of  $Ln^{3+}$  and  $Ce^{3+}$  ions and assumed as a host independent constant given in ref 25. The measured and calculated first 4f–5d transition energies of  $Ln^{3+}$  ions in  $K_3YF_6$  were listed in Table 5. It is straightforward that determining the position of the ground state of  $4f^N$  configuration is the key to labeling out the lowest observed energy positions for  $4f^{N-1}5d$  and  $4f^{N-1}6s$  configurations.

The X-ray photoelectron spectroscopy (XPS) can be used to determine the energy difference between the  $4f^N$  ground state and the top of valence band.<sup>81</sup> However, there are no available XPS data for  $Ln^{3+}$  doped in the  $K_3YF_6$  host up to now. Thus, one better estimation will be alternative based on some reasonable hypotheses. Following the assumption made by Dorenbos in ref 27, the energy position of the  $4f^N$  ground state of any  $Ln^{3+}$  ion relative to the top of the valence band in  $K_3YF_6$  host can be expressed as follows:

$$E_{VF}(Ln^{3+}) = E_{VF}(Ce^{3+}) + \Delta E_{VF}(Ln^{3+}, Ce^{3+}) \quad (18)$$

where  $\Delta E_{VF}(Ln^{3+}, Ce^{3+})$  is assumed to be a host independent constant given by ref 27, and the related values were collected in Table 7. The first term (i.e., the parameter  $E_{VF}(Ce^{3+})$  in host  $K_3YF_6$ ) can be determined by going along the following way. It is well-known that the fine structures of the transitions to higher-energy 5d states of  $Ce^{3+}$  ions will be obscured, which is not mainly because of crystal lattice vibration but attributed to line broadening associated with the reduction of excited-state lifetimes by rapid ionization of the 5d electron into the conduction band.<sup>82</sup> This means the high-lying 5d states are inside the conduction band. By inspecting the fwhm of all the broad bands of the 4f–5d transitions of  $Ce^{3+}$  ions in Figure 8, we found that the fwhm of the bands above  $48\,000 \text{ cm}^{-1}$  are almost twice than those below, and thus, the energy position of the 4f ground state of  $Ce^{3+}$  ions in  $K_3YF_6$  relative to the top of the valence band  $E_{VF}(Ce^{3+})$  was set as  $52\,000 \text{ cm}^{-1}$ . Finally, by employing eq 18 and the values of  $\Delta E_{VF}(Ln^{3+}, Ce^{3+})$  and  $E_{VF}(Ce^{3+})$ , we obtained the energy positions of the  $4f^N$  ground states of all the  $Ln^{3+}$  ions relative to the top of the valence band in  $K_3YF_6$  host and listed them in Table 7.

Under the usage of the energy positions of the  $4f^N$  ground states of  $Ln^{3+}$  ions in the band gap in combination with the calculated lowest 4f–5d and 4f–6s transition energies listed in the Table 5, the lowest energy level positions of  $4f^{N-1}5d$  and  $4f^{N-1}6s$  configurations relative to the top of the valence band ( $E_{VD}(Ln^{3+})$  and  $E_{VS}(Ln^{3+})$ ) were easily obtained and listed in Table 7. A complete understanding of various excitation channels in the band gap of  $K_3YF_6$  host has been schematically shown in Figure 7 by using all the calculated data listed in Table 7.

## ■ COMPARISON OF THE CALCULATED RESULTS WITH EXPERIMENTS

The measured excitation spectra (red full lines) at 8 K and simulated 4f–5d absorption spectra (blue dashed and green dotted lines) of  $Ln^{3+}$  doped in  $K_3YF_6$  host ( $Ln = Ce, Pr, Nd, Eu, Gd, Tb, Dy$ , and  $Er$ ) have been presented in Figures 8–15 where the vertical bars show the calculated energy positions and relative line strengths of ZPLs, and the blue and green colors represent two different sites (dominant Y site and

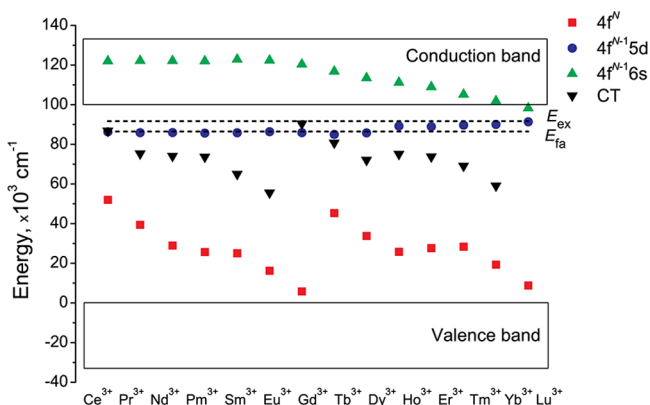


**Figure 7.** Lowest energy level positions of  $4f^N$ ,  $4f^{N+1}(np)^5$ ,  $4f^{N-1}5d$ , and  $4f^{N-1}6s$  configurations relative to the top of valence band in  $K_3YF_6$ .

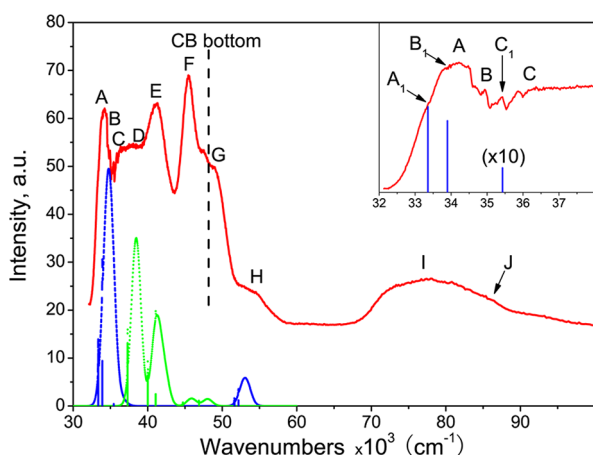


**Figure 8.** Measured excitation and simulated 4f–5d absorption spectra of  $Ce^{3+}$  ions in  $K_3YF_6$ . The inset figure shows the fine structures of lower energy bands A, B, and C, where the calculated intensity of the ZPL  $C_1$  is enlarged by 10 times for better display.

secondary K(1) site) occupied by  $Ln^{3+}$  ions, respectively. More simulation details can be found in the theory section.

**$Ce^{3+}$ .** Figure 8 shows the excitation spectrum of  $Ce^{3+}$  ions doped in  $K_3YF_6$  monitoring the  $5d^1 \rightarrow {}^2F_{7/2}$  emission at 350 nm. There are ten observed broad bands labeled by A–J, where the first three ones have the fine structures consisting of ZPLs and vibronic side bands as shown in the inset of Figure 8. To obtain a much better understanding of 4f–5d transitions of  $Ce^{3+}$  ions, we will have to first separate other excitation channels in the VUV spectra. The band I beginning at about 70 000  $cm^{-1}$  and reaching a maximum at 77 000  $cm^{-1}$  was regarded as the 4f–6s transition, which is consistent with the assignment of  $Ce^{3+}$  doped in  $LaF_3$  (~68 000  $cm^{-1}$ ) made by Elias et al.<sup>28</sup> The observed fact that the bands I and J span about 20 000  $cm^{-1}$  suggests that there are other transition mechanisms different from 4f–6s transition to result in band J. Following our discussions in the foregoing section, the band J around 86 000  $cm^{-1}$  can be attributed to the fundamental absorption of host lattice located at 86 500  $cm^{-1}$  and the CT transition to  $4f^2(np)^5$  configuration whose threshold is estimated as 86 800  $cm^{-1}$  (see Table 5). In addition, the CT transition from the top of the valence band to the 5d lowest state is also possible, whose transition energy is 86 100  $cm^{-1}$  as shown in the Table 7. The surmise not only originates from the

accidental consistency of the calculated results but also has been reported in the  $LiCaAlF_6$  host doped with  $Ce^{3+}$  ions.<sup>83</sup> Therefore, with so many broad excitation channels in the range from 70 000 to 90 000  $cm^{-1}$ , it is no wonder that the whole width of bands I and J is so great.

The eight bands between 30 000 and 60 000  $cm^{-1}$  (i.e., A to H) were assigned as 4f–5d transitions, whose maxima were collected in Table 8. Since the energy structure calculations are

**Table 8.** Measured and Calculated Energies of the 5d States of  $Ce^{3+}$  Ions, Respectively, Situated at the Y and K(1) Sites of  $K_3YF_6$  host (Unit,  $cm^{-1}$ )

site	$E_{\text{exptl(Vib)}}^a$	$E_{\text{exptl(ZPL)}}^a$	$E_{\text{calcd}}^c$	$\Delta_{\text{ZPL}}^b$	CP <sup>d</sup>
Y	34319 (A)	33399 ( $A_1$ )	33354	45	${}^2t_2$
	34937 (B)	33850 ( $B_1$ )	33899	−49	${}^2t_2$
	36576 (C)	35432 ( $C_1$ )	35430	2	${}^2t_2$
			51637		${}^2e$
	53292 (H)	52122	52171	−49	${}^2e$
	38673 (D)	37503	37293	210	${}^2t_2$
	41261 (E)	40091	40004	87	${}^2t_2$
			41073		${}^2t_2$
K(1)	45457 (F)	44287	44719	−432	${}^2e$
	48409 (G)	47239	46876	363	${}^2e$

<sup>a</sup>The symbols  $E_{\text{exptl(Vib)}}$  and  $E_{\text{exptl(ZPL)}}$ , respectively, stand for the energy positions of the vibronic maxima and deduced ZPLs of the observed bands. <sup>b</sup> $\Delta_{\text{ZPL}} = E_{\text{exptl(ZPL)}} - E_{\text{calcd}}$ . <sup>c</sup>The standard deviation can be defined as

$$\sigma = \sqrt{\sum_{i=1, \dots, N_E(\text{cf})} \frac{\Delta_i(\text{ZPL})^2}{(N_E(\text{cf}) - N_p(\text{cf}))}}$$

where the number of the possible experimental energy levels  $N_E(\text{cf})$  and the number of fitting parameters  $N_p(\text{cf})$  are, respectively, 4 and 3. The present calculated standard deviations for the Y and K(1) sites are, respectively, 98 and 649  $cm^{-1}$ . <sup>d</sup>CP, cubic parentage.

always related to the ZPLs, it is desirable to extract as many ZPLs as possible from the excitation spectra. However, only three ZPLs ( $A_1$ ,  $B_1$ , and  $C_1$ ), respectively, at 33 399, 33 850, and 35 432  $cm^{-1}$  were directly found (see the inset of Figure 8).

To overcome this difficulty, Reid and van Pieterse et al.<sup>19,20</sup> assumed that the energy position of any 5d electronic origin can be obtained by subtracting one reasonable constant energy  $E_{\text{shift}}$  (i.e., peak offset from ZPL, and taken as 1170  $cm^{-1}$  for our case) from the maximum of the corresponding vibronic band. Following this assumption, all the possible ZPLs for 5d states of  $Ce^{3+}$  doped in  $K_3YF_6$  were determined and presented in Table 8. By inspecting Table 8, we found that the number of the observed ZPLs exceeded the number of the present 5d CF splittings of  $Ce^{3+}$  ions situated at any single site with  $C_i$  point group symmetry (i.e.,  $8 > 5$ ). The explanation of the additional ZPLs will need to further review the crystal structure of the host in detail. As discussed in the experimental details section, it is possible that  $Ln^{3+}$  ions, especially for the first half of the series, occupy the K(1) site based on the consideration of ionic size (see the Table 1). Meanwhile, the occupation of the Y site is still dominant because a further charge compensation will be required for the K(1) site. This kind of phenomenon of multisite occupation has been observed in  $Li_3YCl_6:Ce^{3+15}$  with similar crystal structures to  $K_3YF_6$  host. Afterward, these ZPLs listed in Table 8 will be assigned to the corresponding sites by analyzing the local structure of every site, and two sets of 5d

Table 9. 5d CFP and CF Strength Values for 5d Ce<sup>3+</sup> Ions at the Y, K(1), and K(2) Sites of K<sub>3</sub>YF<sub>6</sub> (Units, cm<sup>-1</sup>)

	K <sub>3</sub> YF <sub>6</sub>								
	Y site			K(1) site			K(2) site		
	B <sub>q</sub> <sup>(pc)k</sup>	B <sub>q</sub> <sup>(ec)k</sup>	total	B <sub>q</sub> <sup>(pc)k</sup>	B <sub>q</sub> <sup>(ec)k</sup>	total	B <sub>q</sub> <sup>(pc)k</sup>	B <sub>q</sub> <sup>(ec)k</sup>	total
B <sub>0</sub> <sup>2</sup> (d)	-25	-870	-895	-420	-1491	-1911	-901	-4774	-5675
B <sub>1</sub> <sup>2</sup> (d) <sup>a</sup>	-428 - i1046	787 + i2022	359 + i976	426 - i135	-353 - i2975	74 - i3110	-197 - i1329	50 - i533	-146 - i1862
B <sub>2</sub> <sup>2</sup> (d) <sup>a</sup>	-276 - i274	1197 - i290	921 - i564	-65 - i389	-1421 - i3893	-1486 - i4282	-411 + i692	-783 + i4290	-1194 + i4982
B <sub>0</sub> <sup>4</sup> (d)	-13039	30021	16982	-877	7126	6249	1610	-1960	-350
B <sub>1</sub> <sup>4</sup> (d) <sup>a</sup>	16902 - i7643	-36374 + i16849	-19472 + i9206	-715 + i401	6194 - i1979	5479 - i1578	-175 + i135	-96 - i224	-271 - i89
B <sub>2</sub> <sup>4</sup> (d) <sup>a</sup>	-1580 + i6175	3471 - i13019	1891 - i6844	-253 - i157	1181 - i570	928 - i727	253 - i284	-643 + i2537	-390 + i2253
B <sub>3</sub> <sup>4</sup> (d) <sup>a</sup>	7297 - i5326	-15790 + i12376	-8493 + i7050	-317 - i449	2262 - i2072	1945 - i2521	23 - i183	13 + i317	36 + i134
B <sub>4</sub> <sup>4</sup> (d) <sup>a</sup>	9635 - i13090	-21847 + i28167	-12212 + i15077	584 - i593	-4885 + i4572	-4301 + i3979	-1261 + i193	-25 - i3871	-1286 - i3678
N <sub>v</sub> (B <sup>2</sup> (d)) <sup>b</sup>			3648			12692			15178
N <sub>v</sub> (B <sup>4</sup> (d)) <sup>b</sup>			56837			16534			7579
N <sub>v</sub> (d) <sup>b</sup>			56954			20844			16965

<sup>a</sup>The CFPs for  $q < 0$  are related to ones for  $q > 0$  by  $B_{-q}^k(d) = (-1)_q B_q^k(d)$ . <sup>b</sup> $N_v(B^2(d))$ ,  $N_v(B^4(d))$ , and  $N_v(d)$  are, respectively, the second and fourth rank and total CF strength parameters defined by Auzel et al.<sup>38</sup>

CFPs, respectively, for the Y and K(1) sites, will be produced by fitting these ZPLs based on ECM.

For the Y site, the almost perfect octahedral coordination by six F<sup>-</sup> ions leads to that the 5d orbitals of Ce<sup>3+</sup> ions are split into two sets <sup>2</sup>e and <sup>2</sup>t<sub>2</sub>, with <sup>2</sup>t<sub>2</sub> being lower in energy. The energy separation between <sup>2</sup>e and <sup>2</sup>t<sub>2</sub> is very large and can be estimated as ~19 000 cm<sup>-1</sup> from the CF splitting of Ce<sup>3+</sup> ion in Rb<sub>2</sub>NaYF<sub>6</sub><sup>84</sup> due to the similar interionic distance between the Y<sup>3+</sup> and F<sup>-</sup> ions (about 2.1704 Å<sup>85</sup>). The 5d spin-orbit coupling interaction and small CF distorted interaction deviated from O<sub>h</sub> only induce <sup>2</sup>t<sub>2</sub> and <sup>2</sup>e orbitals, respectively, into three and two CF energy levels, whose splittings are very small and have the magnitude order of 10<sup>3</sup> cm<sup>-1</sup>. For the K(1) site, the distortion deviated from O<sub>h</sub> is great, and the interionic distance between K<sup>+</sup> and F<sup>-</sup> ions is much bigger (about 2.63 Å<sup>10</sup>), which results in that the admixture of <sup>2</sup>e and <sup>2</sup>t<sub>2</sub> cubic parentages are strong for every 5d CF state and that the energy difference between the two outermost CF energy levels is much smaller than that for the Y site. According to the above judgments from the crystal structure of the host in combination with the observed energy positions of all the ZPLs listed in Table 8, the bands A, B, C, and H were assigned to the Y site, whereas the bands D, E, F, and G were attributed as the K(1) site.

Three G parameters in ECM must be reduced to two because the number of the G parameters plus Δ<sub>E</sub>(fd) must be less than the number of the deduced ZPLs (i.e., 4) in the whole fitting procedure where the 5d spin-orbit coupling parameter is fixed to the known value listed in Table 2. Following the assumption for G parameters of d electron proposed in ref 52, the values of G<sub>s</sub> and G<sub>σ</sub> are assumed to be the same (i.e., G<sub>s</sub> = G<sub>σ</sub> = G<sub>ss</sub>). By employing ECM in combination with the preliminary preparation works in the section where determination of parameter values and simulation of spectra were done, we got two sets of G and Δ<sub>E</sub>(fd) parameter values, respectively, for the Y and K(1) sites: G<sub>ss</sub>(Y) = 2.41, G<sub>π</sub>(Y) = 2.41, and Δ<sub>E</sub>(fd, Y) = 39 332 cm<sup>-1</sup>; G<sub>ss</sub>(K(1)) = 3.52, G<sub>π</sub>(K(1)) = 9.59, and Δ<sub>E</sub>(fd, K(1)) = 40 536 cm<sup>-1</sup>. The standard fitting deviations for the Y and K(1) sites are 98 and

649 cm<sup>-1</sup>. The present obtained G parameter values are very similar with the reported values for Ce<sup>3+</sup> ions in LiYF<sub>4</sub> in ref 55. It is not strange that the contribution from the exchange charge (i.e., G parameter values) becomes much bigger because the partial contribution of the exchange charge has been used to cancel the effect caused by the negative β<sub>4</sub> coefficients<sup>55</sup> in the point charge term. In addition, the calculated Δ<sub>E</sub>(fd) parameter values are around 40 000 cm<sup>-1</sup> and very close to that of Ce<sup>3+</sup> ions in LiCaAlF<sub>6</sub><sup>86</sup> due to the similar slightly distorted octahedral coordination by six F<sup>-</sup> ions. The above agreements show fairly well that our site assignment of ZPLs listed in Table 8 is reasonable. Three sets of calculated 5d CFPs of Ce<sup>3+</sup> ions for the Y, K(1), and K(2) sites were collected in the Table 9, where those for the K(2) site were evaluated only for comparison by using the obtained G parameter values of the K(1) site. To compare the 5d CF effects of various sites, the 5d CF strength parameters of Ce<sup>3+</sup> situated at different sites were calculated and also collected in Table 9. It is deduced from Table 9 that the orders of the total and second rank CF strengths of three sites show that the Y site has more compact coordination environment with closely perfect O<sub>h</sub> symmetry and the reason why the K(2) site is not a good position to be occupied by Ln<sup>3+</sup> ions is the weaker 5d CF environment of the K(2) site except for the small coordination number. Finally, the calculated 5d CF energy levels of Ce<sup>3+</sup> ions situated at Y and K(1) sites were listed in Table 8 for further comparison with the experimental values.

Figure 8 shows that the simulated absorption spectrum basically agrees with the measured excitation one except for the calculated absorption intensities of bands F and G. The imperfection of our simulation can be explained as the fact that the highly efficient radiative energy transfer between excitons and luminescent Ce centers, namely, that Ce centers situated in Y site absorb the STE emission,<sup>82,87</sup> improves the excitation intensities of bands F and G very close to the conduction band and excitonic absorption position as shown in Figure 8.

**Pr<sup>3+</sup>.** Figure 9 shows the excitation spectrum of Pr<sup>3+</sup> ions doped in K<sub>3</sub>YF<sub>6</sub> monitoring the <sup>3</sup>P<sub>0</sub> → <sup>3</sup>H<sub>4</sub> emission at 482 nm. After comparing the excitation spectrum of Pr<sup>3+</sup> ion in K<sub>3</sub>YF<sub>6</sub>

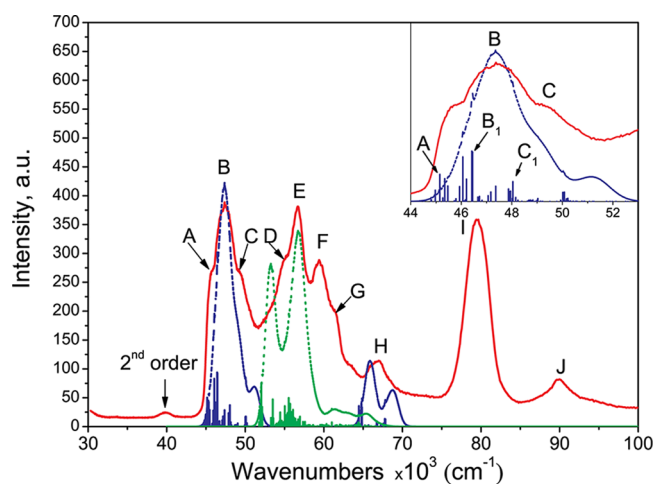


**Figure 9.** Measured excitation and simulated 4f–5d absorption spectra of  $\text{Pr}^{3+}$  ions in  $\text{K}_3\text{YF}_6$ . The inset shows the simulation detail of the first 4f–5d transition band.

with that of  $\text{Ce}^{3+}$  ion in the same host and considering the energy position of the first 4f–5d transition of the  $\text{Pr}^{3+}$  ion predicted by Table 5, the eight bands between 45 000 and 70 000  $\text{cm}^{-1}$  labeled by A–H were determined to be associated with  $4f^2 \rightarrow 4f5d$  transitions. On the left of the 4f–5d transition regions, the weak band around 40 000  $\text{cm}^{-1}$  was observed and assigned as the second order process of the strong band I at  $\sim 80\,000\text{ cm}^{-1}$  because the transition energy value of this band was just half of that of band I. The present CF calculations for  $4f^2$  configuration of the  $\text{Pr}^{3+}$  ions in  $\text{K}_3\text{YF}_6$  show that there are no energy levels of  $4f^2$  configuration located in this energy range as the extended Dieke's diagram described in refs 71 and 73. At the higher energy direction, the CT transition,  $4f^2 \rightarrow 4f6s$  transition, and host lattice absorption will compete with each other and form various broad bands. The strong band I was more likely attributed as the CT transition because the CT transition intensity is generally much larger, and its band maximum is just located between the predicted onset and maximum values of CT transition in Table 5. The 4f–6s transition predicted at  $82\,800\text{ cm}^{-1}$  is also possibly existent, but this transition band will be buried or hidden by the stronger CT transition band due to the weaker 4f–6s transition intensity induced by the small wavefunction admixture with 4f5d states. Moreover, the predicted 4f–6s transition energy is similar to the assignment of  $\text{Pr}^{3+}$  doped in  $\text{LaF}_3$  ( $\sim 80\,000\text{ cm}^{-1}$ ),<sup>28</sup> which also proves that our theoretical scheme is universal just as the Dorenbos's formula describing the energy position of the first 4f–5d transition.<sup>24,25</sup> Since the final band J starts at  $\sim 87\,000\text{ cm}^{-1}$  and reaches the maximum at  $90\,000\text{ cm}^{-1}$ , it was thought to be very typically associated with the host absorption. In addition, the highest excited state  $^1S_0$  of the  $4f^2$  configuration of the  $\text{Pr}^{3+}$  ion doped in fluorides has attracted more attention due to the potential applications in quantum cutting.<sup>88</sup> The occurring condition of two photon emission of the  $\text{Pr}^{3+}$  ion is that the  $^1S_0$  state must be located below the lowest energy level of the 4f5d configuration. The present CF calculations of the  $4f^2$  and 4f5d configuration for the Y and K(1) sites show that the  $^1S_0$  state of the Y site located at  $47\,485\text{ cm}^{-1}$  is buried in the 4f5d configuration (see the Figure 9), whereas the  $^1S_0$  state of the K(1) site located at  $46\,874\text{ cm}^{-1}$  is far away from the lowest energy level of the 4f5d configuration located at  $51\,758\text{ cm}^{-1}$ . This means that the photon cascade emission can be

observed only for  $\text{Pr}^{3+}$  ions situated at the K(1) site under the suitable site selective excitation. Such prediction is consistent with the reported results of  $\text{Cs}_2\text{KYF}_6:\text{Pr}^{3+}$ ,<sup>13</sup> and further spectral measurements can confirm it.

Following the assignments of site attributions of 4f–5d transition bands of  $\text{Ce}^{3+}$  ions in  $\text{K}_3\text{YF}_6$ , the bands with maxima at  $45\,633\text{ cm}^{-1}$  (A),  $47\,349\text{ cm}^{-1}$  (B),  $49\,234\text{ cm}^{-1}$  (C), and  $66\,852\text{ cm}^{-1}$  (H) were assigned to the Y site, whereas the bands with maxima at  $54\,895\text{ cm}^{-1}$  (D),  $56\,551\text{ cm}^{-1}$  (E),  $59\,428\text{ cm}^{-1}$  (F), and  $61\,335\text{ cm}^{-1}$  (G) were attributed as the K(1) site. For the Y site, the bands A–C and H, respectively, correspond to the transitions to the high spin states  $^3[^2F, ^2t_2]$  and  $^3[^2F, ^2e]$  of 4f5d configuration (where the symbols denote the  $4f^1$  core  $^{2S+1}L$  states and the cubic parentages of the 5d CF states upon the Y site symmetry). The three bands A–C were plotted in more detail to show the further splitting caused by the 4f–5d Coulomb interaction; the remaining CF perturbation term deviated from  $O_h$  cubic CF interaction and the spin–orbit coupling interactions of  $4f^1$  core and 5d single electron in the inset of Figure 9. It is seen from the inset figure that the biggest contribution to intensity of band A originates from these ZPLs calculated at  $\sim 45\,200\text{ cm}^{-1}$ , the bands B and C are the vibronic maxima of calculated pure transitions  $B_1$  and  $C_1$ , respectively, placed at  $\sim 46\,200$  and  $\sim 48\,000\text{ cm}^{-1}$ , and the next vibronic band formed by the calculated ZPLs around  $50\,000\text{ cm}^{-1}$  can be not observed due to being buried by the band C and the onset of the next band D. The transition to  $^2e$  CF component (i.e., band H) seems also to be split as our calculation shows, but the rapid ionization of the 5d electron into conduction band<sup>82</sup> directly makes the high-lying band H broad so as to obscure any splitting detail. For the K(1) site, the bands D, E, F, and G are assigned to transitions to, respectively, the first, second, fourth, and fifth 5d CF components in comparison with the four observed 5d CF components of  $\text{Ce}^{3+}$  ions situated at the K(1) sites in  $\text{K}_3\text{YF}_6$ . The splitting details caused by the 4f–5d Coulomb and  $4f^1$  and 5d spin–orbit coupling interactions become unclear due to the competitive activities of the much larger remained CF term deviated from  $O_h$  cubic CF interaction in the K(1) site as the parameter values of the second rank CF strength of the K(1) site show in Table 9.

In Figure 9, the simulated absorption spectrum for the Y site fairly well agrees with measured excitation spectrum. For the K(1) site, the calculated spectrum also coincides with the experimental one, but the simulation of intensities of bands F and G is not good. This can be understood as the same mechanism occurring in failed simulation of the bands F and G of  $\text{Ce}^{3+}$  ions in  $\text{K}_3\text{YF}_6$ .

**$\text{Nd}^{3+}$ .** The excitation spectrum of  $\text{Nd}^{3+}$  ions doped in  $\text{K}_3\text{YF}_6$  monitoring the emission starting from the lowest energy level of  $4f^25d$  configuration at  $190\text{ nm}$  is presented in Figure 10. The host absorption, CT transition, and  $4f^3 \rightarrow 4f^26s$  transition bands, respectively, predicted at  $86\,500$ ,  $74\,100$ , and  $93\,200\text{ cm}^{-1}$  are not found where the last one competitive channel is not under consideration due to being covered by the host absorption. The vanishing reason of the first two high-energy excitation channels in the excitation spectrum can be explained as the inefficient energy transfer from these strong absorption energy states to the lowest  $4f^25d$  emitting energy states of  $\text{Nd}^{3+}$  ions in  $\text{K}_3\text{YF}_6$ .

The five excitation bands labeled by A–E are associated with transitions from the  $\text{Nd}^{3+}I_{9/2}$  ground state to various  $4f^25d$  energy states. Our previous work<sup>11</sup> compared the onset and maximum of these excitation bands and Stokes shifts with other



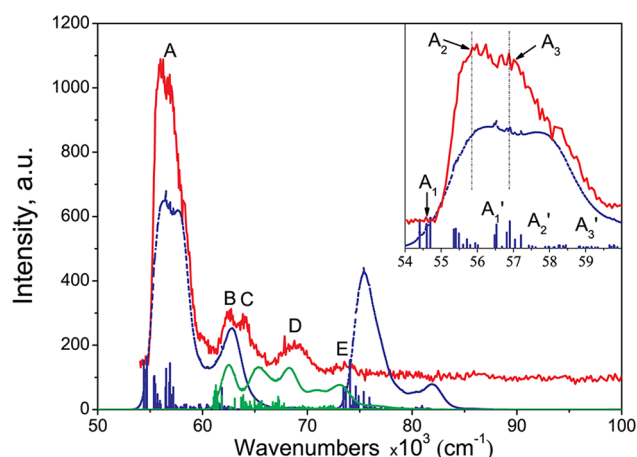


**Figure 10.** Measured excitation and simulated 4f–5d absorption spectra of  $\text{Nd}^{3+}$  ions in  $\text{K}_3\text{YF}_6$ . The inset shows the fine structure of the first 4f–5d transition band.

fluoride hosts, such as  $\text{LiYF}_4$ , and found the much larger lattice coupling effect relative to other fluoride hosts further intensified the structureless character of the 4f–5d excitation bands. This suggests that it is possible to understand various 4f–5d excitation bands of  $\text{Nd}^{3+}$  ions in the  $\text{K}_3\text{YF}_6$  host by using a rough model only with the consideration of the Coulomb interaction of the  $4f^2$  core and 5d CF interaction. Thus, the energy level structure of  $4f^25d$  configuration of  $\text{Nd}^{3+}$  ions in  $\text{K}_3\text{YF}_6$  can be regarded as the term of  $4f^2$  core coupling with every 5d crystal field component, i.e.,  $^{2S+1}[^{2S+1}L_{\beta} \ ^2\Gamma_d]$  (where  $\Gamma_d$  is the irreducible representation of the 5d crystal field component, and  $S$  is the total spin quantum number equal to  $S_f + 1/2$  or  $S_f - 1/2$ ). Not all the transitions from the  $^4I_{9/2}$  ground state to the  $4f^25d$  energy states can be allowed since the standard electric-dipole selection rule given by ref 46 or 89 requires  $S = 3/2$  and  $3 \leq L_f \leq 9$ . Upon the inspection of various terms of the  $4f^2$  configuration, only transitions to these final states  $^4[{}^3H; {}^2\Gamma_d]$  and  $^4[{}^3F; {}^2\Gamma_d]$  can be observed in the 4f–5d excitation spectrum. For the Y site, the 5d CF components  $\Gamma_d$  can be approximately written as  $t_2$  and  $e$ , and thus there should be four vibronic bands to be possibly measured as shown in our simulated vibronic bands plotted with the blue dashed line in Figure 10. This gives a better and simple physics understanding to our CF calculations and experimental assignments.

There is no doubt that the band A with maximum at  $\sim 56\,800\text{ cm}^{-1}$  is associated with the Y site and assigned to  $^4[{}^3H; {}^2t_2]$  due to the predicted onset by Dorenbos's formula and the lowest energy term  ${}^3H$  of  $4f^2$  core. The next band B with maximum at  $62\,261\text{ cm}^{-1}$  can be attributed as  $^4[{}^3F; {}^2t_2]$  because the energy separation between the maxima of bands A and B is very similar to the energy difference between  ${}^3H$  and  ${}^3F$  terms of  $4f^2$  configuration of  $\text{Pr}^{3+}$  ions approximately read from the Dieke's diagram. The two transitions to the high energy  $e$  orbit coupling with  ${}^3H$  and  ${}^3F$  core terms is expected at  $\sim 75\,400$  and  $\sim 81\,000\text{ cm}^{-1}$ , according to our CF calculations or the 5d CF splitting derived from the excitation bands of  $\text{Ce}^{3+}$  ions situated at the Y sites. However, in these energy regions, the predicted CT transition intensity is so large that the corresponding 4f–5d transitions can not be found. In addition, the less efficient energy transfer from these energy positions to the lowest luminescent  $4f^25d$  levels will also weaken the intensities of the predicted 4f–5d intense bands because the 5d–4f radiative

behaviors are more dominant for these much higher-lying  $4f^25d$  energy levels.

To display fairly well the relatively fine splitting caused by other possibly big interactions, the band A was enlarged and replotted in the inset of Figure 10. It is impossible to observe the energy splitting between the HS and LS states of  $4f^25d$  caused by the 4f–5d Coulomb interaction in the excitation spectrum of  $\text{Nd}^{3+}$  ions because the almost forbidden transitions from  $^4I_{9/2}$  ground state to low-spin  $1/2$  states are always buried in the strong vibronic bands of SA transitions, but the spin–orbit coupling splitting of the  $4f^2$  core can be clearly distinguished in the first 4f–5d excitation band. According to our CF calculations, the first 4f–5d excitation band actually includes three typical groups of the calculated ZPLs labeled by  $A_1$ – $A_3$ , whose barycenters are, respectively, located at  $54\,580$ ,  $55\,835$ , and  $57\,031\text{ cm}^{-1}$ . Their energy separations are consistent with the calculation results of the spin–orbit coupling splitting of  $4f^2$  core within the first 4f–5d excitation band of  $\text{Nd}^{3+}$  ions in  $\text{YPO}_4$  shown in ref 90, which provides the direct evidence to confirm the origin of these splittings in the first 4f–5d excitation band. Although the 5d spin–orbit interaction is weaker than the 4f spin–orbit interaction, its splitting effect can also be observed. The energy splitting between  $\Gamma_7$  and  $\Gamma_8$  induced from  ${}^2t_2$  by the 5d spin–orbit interaction can be estimated as about  $1800\text{ cm}^{-1}$  if the 5d spin–orbit parameter of  $\text{Nd}^{3+}$  ions is used. This means the six groups of ZPLs can be expected in the band A where another three groups of ZPLs can be approximately displaced from  $A_1$ – $A_3$  by  $1800\text{ cm}^{-1}$ , as these ZPLs marked with  $A'_1$ – $A'_3$  show in the inset of Figure 10. The abundant observed ZPLs and vibronic progresses in the first 4f–5d excitation band A fairly well show the validity of our physics understanding of the energy splittings caused by the 5d and  $4f^2$  core spin-coupling interaction.

For the K(1) site, the magnitude order of 5d CF splitting is not much more than that of the energy splitting inside of  $4f^2$  core, and thus, the admixture of various quantum numbers is strong. The previous assumption of  $4f^2$  core coupling with 5d CF components is no longer a good model so that the understanding of the 4f–5d transitions of the K(1) site will have to depend on the full CF calculations. The related simulated vibronic bands plotted in Figure 10 agree with the observed bands with maxima at  $62\,261\text{ cm}^{-1}$  (B),  $64\,017\text{ cm}^{-1}$  (C),  $68\,567\text{ cm}^{-1}$  (D), and  $73\,376\text{ cm}^{-1}$  (E) very well. It is noted that the Y and K(1) sites maybe both have the contributions to the intensity of the band B, and the band E can be understood as the superposition of ZPLs of the Y site and vibronic bands of the K(1) site.

**$\text{Eu}^{3+}$ .** Figure 11 shows the excitation spectrum of  $\text{Eu}^{3+}$  ions doped in  $\text{K}_3\text{YF}_6$  monitoring the  ${}^5D_0 \rightarrow {}^7F_1$  emission at  $592\text{ nm}$ . The maximum of the host absorption (i.e., band G) is observed at  $\sim 90\,000\text{ cm}^{-1}$ , which is consistent with the previous assignments of other  $\text{Ln}^{3+}$  ions doped in the same host lattice. By referring to the Table 5, the lowest energy  $4f^6 \rightarrow 4f^66s$  transition was predicted at ca.  $106\,000\text{ cm}^{-1}$  and thus can not be observed in the excitation spectrum because its transition energy is much more than the fundamental absorption energy of the host lattice  $E_{\text{fa}}$ . For  $\text{Eu}^{3+}$  ions in solid, the CT transition energy is always much lower than the 4f–5d transition energies. Therefore, the first broad band A whose maximum is at  $\sim 63\,700\text{ cm}^{-1}$  was assigned as the CT transition without any hesitation.

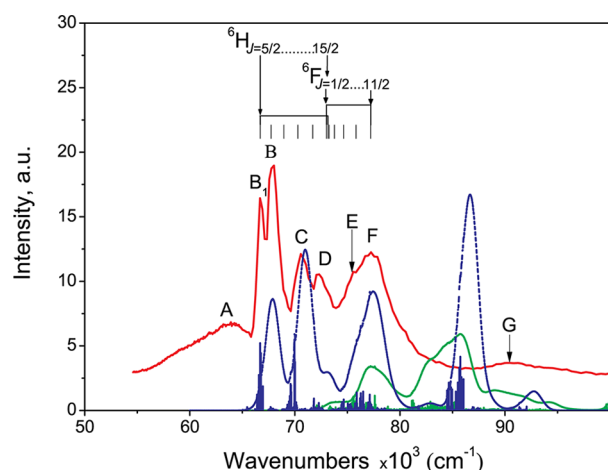


**Figure 11.** Measured excitation and simulated 4f–5d absorption spectra of  $\text{Eu}^{3+}$  ions in  $\text{K}_3\text{YF}_6$ .

By following the position prediction of the lowest 4f–5d transition of  $\text{Eu}^{3+}$  ions given by Dorenbos (i.e., referring to the value in Table S), the first 4f–5d transition is associated with the Y site and assigned at  $66\,706\text{ cm}^{-1}$  ( $B_1$ ). The next observed bands with maxima at  $67\,878\text{ cm}^{-1}$  (B),  $70\,438\text{ cm}^{-1}$  (C),  $72\,203\text{ cm}^{-1}$  (D),  $75\,344\text{ cm}^{-1}$  (E), and  $77\,302\text{ cm}^{-1}$  (F) are also attributed as the 4f–5d transitions. Our simulated 4f–5d transition vibronic bands, respectively, for the Y and K(1) sites in Figure 11 show that the latter (the green dotted line) are always buried by the former (the blue dashed line). Moreover, the Y site is always dominant in the substituting process of  $\text{Ln}^{3+}$  ions. Therefore, the two facts suggest the bands B–E can be assigned to the Y site. Nevertheless, the much larger experimental bandwidth of band E and its long tail might imply the existence of the 4f–5d excitation of  $\text{Eu}^{3+}$  ion situated at the K(1) site. As a conservative consideration, the band E was explained as the superposition of the vibronic bands of  $\text{Eu}^{3+}$  ions situated at two sites.

According to the 5d CF splitting derived from the excitation bands of  $\text{Ce}^{3+}$  ions situated at the Y site and the first 4f–5d transition energy position with the 5d CF component  $t_2$  (i.e.,  $B_1$ ), the lowest energy state with the high-energy 5d CF component e is expected at  $\sim 85\,000\text{ cm}^{-1}$ , as the simulated vibronic band around  $86\,628\text{ cm}^{-1}$  shows. However, the predicted intense 4f–5d absorption band unfortunately meets the threshold of the host absorption around  $86\,500\text{ cm}^{-1}$  and thus can not be observed in the excitation spectrum. The similar situation also falls upon the high-energy simulated vibronic bands of  $\text{Eu}^{3+}$  ions situated at the K(1) site (i.e., the band plotted with the green dotted line at  $\sim 85\,000\text{ cm}^{-1}$ ). Thus, the bands B–F are associated with the 5d CF component  $t_2$  of the Y site in nature.

Upon the basis of the rude model used to understand 4f<sup>5</sup>5d energy structure of  $\text{Nd}^{3+}$  ions in the above section, the bands B–F actually reflect the splitting of 4f<sup>5</sup> core by the Coulomb and spin–orbit coupling interactions. The similar symbols  $7[{}^{2S+1}L_f; {}^2\Gamma_d]$  (having the same total spin quantum number with the initial transition state  ${}^7F_0$  of 4f<sup>6</sup> configuration) can be employed to mark these bands. The lower energy structure of 4f<sup>5</sup> configuration of  $\text{Sm}^{3+}$  ion doped in the  $\text{LaF}_3$  generated by free ion calculation using the free ion parameters reported in ref 17 was plotted in Figure 11 where energy position of the ground state  ${}^6H_{5/2}$  was set at the  $B_1$  position for better

comparison. By inspecting the splitting of the 4f<sup>5</sup> core shown in Figure 11, various bands can be assigned as the following: B–D,  $7[{}^6H; {}^2t_2]$ , and E–F,  $7[{}^6F; {}^2t_2]$ . To well discuss the origin of the energy splitting of the bands B–D and E–F, the idea of the simple model proposed by Duan and Reid<sup>91</sup> will be introduced. The spin–orbit coupling interaction of 4f<sup>5</sup> core will further split  $7[{}^6H; {}^2t_2]$  into several energy levels denoted by  $[({}^{S/2}, {}^{sd}){}^7H_J; t_2]$  ( $J = 2, 3, \dots, 8$ ), where  $J$  is the quantum number of the angular momentum  $J = S + L_f$  in which  $S$  is the total spin, and  $L_f$  is the total orbit angular momentum of  $N - 1$  4f electrons. Since the initial transition state is  ${}^7F_0$  of 4f<sup>6</sup> configuration and the approximate selection rule given by the simple model<sup>89</sup> requires  $|J' - 3| \leq J \leq J' + 3$  ( $J'$  is the total angular momentum of the initial transition state), only the energy state  $[({}^{S/2}, {}^{sd}){}^7H_J; t_2]$  with  $J = 3$  can be observed in the excitation spectrum. This seems to have a conflict with the observed fact that there are two strong bands B and C. Actually, the appearance of the bands B and C is not related to the splitting of the 4f<sup>5</sup> core, but caused by the 5d spin–orbit interaction because the energy splitting caused by the 5d spin–orbit interaction for the low-energy 5d state  ${}^2t_2$  can be estimated as about  $2100\text{ cm}^{-1}$  and very similar to the energy difference between the maxima of the bands B and C if the 5d spin–orbit parameter of  $\text{Eu}^{3+}$  ions is used. Thus, the bands B and C can be assigned as the splittings of  $[({}^{S/2}, {}^{sd}){}^7H_3; t_2]$  caused by the 5d spin–orbit interaction. The weak band D can be explained as the transition to the state  $[({}^{S/2}, {}^{sd}){}^7H_J; t_2]$  with  $J \neq 3$  including the small mixing of  $[({}^{S/2}, {}^{sd}){}^7H_3; t_2]$  induced by the 4f–5d Coulomb interaction except the isotropic exchange part because the direct Coulomb interaction and the anisotropic exchange Coulomb interaction between 4f and 5d electrons do not completely cancel each other. The assignment for the bands B–C can be similarly applied to the bands E and F. In other words, the bands E and F can also be understood as the splittings of  $[({}^{S/2}, {}^{sd}){}^7F_3; t_2]$  caused by the 5d spin–orbit interaction. After all, our CF calculations and related physics picture reproduce the experimental excitation of  $\text{Eu}^{3+}$  ions in  $\text{K}_3\text{YF}_6$  very well as shown in Figure 11.

**Gd<sup>3+</sup>.** Figure 12 shows the excitation spectrum of  $\text{Gd}^{3+}$  ions doped in  $\text{K}_3\text{YF}_6$  monitoring  ${}^6G_{7/2} \rightarrow {}^6P_{7/2}$  emission at 598 nm. At the high energy direction, the band E starts at  $\sim 87\,000\text{ cm}^{-1}$  and reaches the maximum at  $88\,279\text{ cm}^{-1}$ , which agrees with the behavior of the host absorption. Thus, it can be attributed as the host absorption without any question. In addition, the

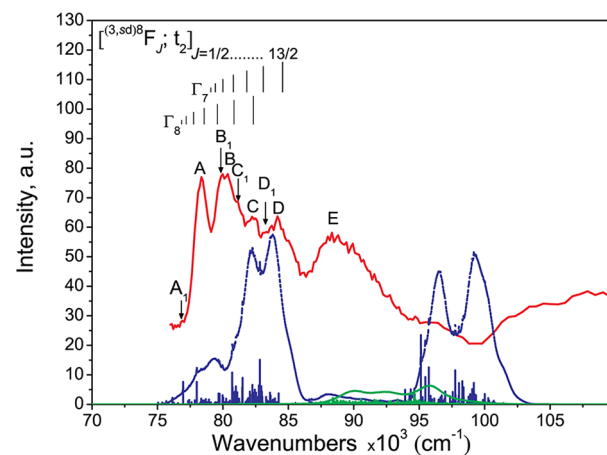


**Figure 12.** Measured excitation and simulated 4f–5d absorption spectra of  $\text{Gd}^{3+}$  ions in  $\text{K}_3\text{YF}_6$ .

intensity of the host absorption begins to decrease above  $88\,778\text{ cm}^{-1}$ . This might be due to inefficient energy transfer from the exciton or conduction band to the present monitoring luminescent state of  $\text{Gd}^{3+}$  and also suggests the excitation intensities of those  $4f^65d$  energy levels close to the exciton absorption position, and the conduction band might also be not very large. The CT and  $4f^7 \rightarrow 4f^66s$  transitions of  $\text{Gd}^{3+}$  ions can not be observed in the excitation spectrum since their predicted transition energies are much more than the transition energy of the host absorption.

Our simulated  $4f-5d$  vibronic bands for the K(1) site plotted with the green dotted line in Figure 11 show that they can not be observed due to lying above the edge of the host absorption. Thus, the bands A–D between  $75\,000$  and  $87\,000\text{ cm}^{-1}$  can be assigned to the  $4f-5d$  transition bands associated with the Y site. The following three states  $^8[{}^7F; {}^2t_2]$ ,  $^6[{}^5D; {}^2t_2]$ , and  $^8[{}^7F; {}^2e]$  are usually the transition final states of the observed  $4f-5d$  excitation bands. However, the last two states have been buried by the host absorption for our case since their energy positions can be, respectively, estimated as  $97\,500$  and  $99\,500\text{ cm}^{-1}$  by referring to the approximate energy separation between  ${}^7F$  and  ${}^5D$  terms of the  $4f^6$  configuration of  $\text{Eu}^{3+}$  ion in the Dieke's diagram, the first  $4f-5d$  transition energy in Table 5, and the  $5d$  CF splitting between  $t_2$  and  $e$  CF components derived from the excitation bands of  $\text{Ce}^{3+}$  ions situated at the Y site. Moreover, the transition from the initial ground state  $^8F_{7/2}$  of  $4f^7$  configuration to  $^6[{}^5D; {}^2t_2]$  is SF. It is seen from Figure 12 that our theoretical calculations and simulations are consistent with the above judgments. Therefore, we finally assigned the bands below  $87\,000\text{ cm}^{-1}$  to the  $4f-5d$  transition to  $^8[{}^7F; {}^2t_2]$ .

The  $4f-5d$  transition to  $^8[{}^7F; {}^2t_2]$  consists of four broad bands including fine structures with maxima at  $78\,451\text{ cm}^{-1}$  (A),  $80\,379\text{ cm}^{-1}$  (B),  $82\,341\text{ cm}^{-1}$  (C), and  $84\,148\text{ cm}^{-1}$  (D). The detailed analyses show four ZPLs are, respectively, located at  $76\,850\text{ cm}^{-1}$  ( $A_1$ ),  $79\,880\text{ cm}^{-1}$  ( $B_1$ ),  $81\,041\text{ cm}^{-1}$  ( $C_1$ ), and  $83\,287\text{ cm}^{-1}$  ( $D_1$ ). These features are due to the splitting of  $^8[{}^7F; {}^2t_2]$  mainly caused by the  $4f^6$  core and  $5d$  spin–orbit interactions. According to the simple model,<sup>91</sup>  $^8[{}^7F; {}^2t_2]$  is split into several energy levels denoted by  $[({}^{3,5d})^8F_J; t_2]$  ( $J = 1/2, 3/2, 13/2$ ) by the  $4f^6$  core spin–orbit interaction, and then any  $[({}^{3,5d})^8F_J; t_2]$  is further approximately split into two energy levels by the  $5d$  spin–orbit interaction whose splitting is about  $\sim 2200\text{ cm}^{-1}$  if the  $5d$  spin–orbit parameter of  $\text{Gd}^{3+}$  ion was used. Two groups of the energy splittings of  $^8[{}^7F; {}^2t_2]$  caused by the  $4f^6$  core spin–orbit interactions, respectively, named by  $\Gamma_8$  and  $\Gamma_7$  have been schematically shown in the Figure 12. The  $\Gamma_7$  group is displaced from the  $\Gamma_8$  group by  $2200\text{ cm}^{-1}$  upward high-energy direction as a whole, and the energy splitting caused by the  $4f^6$  core spin–orbit interaction can be obtained by enlarging the similar energy splitting of  $^8[{}^7F; {}^2e]$  of the  $4f^65d$  configuration of  $\text{Eu}^{2+}$  ions in  $\text{CaF}_2$  shown in Figure 1 of ref 91 by the ratio between the  $4f^6$  core spin–orbit parameters of  $\text{Gd}^{3+}$  and  $\text{Eu}^{2+}$  ions (i.e.,  $\zeta_f(f, \text{Gd}^{3+})/\zeta_f(f, \text{Eu}^{2+})$ <sup>92</sup>). The energy position of the lowest level of the two groups of energy splittings was set at the  $A_1$  ZPL. All the observed ZPLs agree with the understanding of the physics picture and our theoretical calculation results (see Figure 12).

The band structure of the  $4f-5d$  transition to  $^8[{}^7F; {}^2t_2]$  in this host is very different from that to  $^8[{}^7F; {}^2e]$  (at the low-energy side) in  $\text{LiYF}_4$  reported in ref 56. The former has the structure like the lambdoidal ladder and begins to go downward when reaching the maximum, whereas the latter shows the

staircase structure with intensity increasing from low energy to high energy, as any group of the predicted energy splitting given by the simple model in the Figure 12 shows. It is not hard to understand the latter since the  $5d$  spin–orbit interaction does not cause any splitting for  $^8[{}^7F; {}^2e]$ . For the former, if two groups of the calculated intensities with the same energy splitting in Figure 12 are superposed, the structure of the lambdoidal ladder is possible. However, the observed fact that the band intensities at the high-energy side are rapidly decreasing is not consistent with the superposed calculation results. The mismatch can be explained by the fact that the exciton and conduction band around these high-lying energy states (see Figure 7) can easily weaken the energy transfer to the present monitoring luminescent state of  $\text{Gd}^{3+}$ .

**Tb<sup>3+</sup>.** Figure 13 shows the excitation spectrum of  $\text{Tb}^{3+}$  ions doped in  $\text{K}_3\text{YF}_6$  monitoring  ${}^5D_4 \rightarrow {}^7F_5$  emission at  $541\text{ nm}$ .

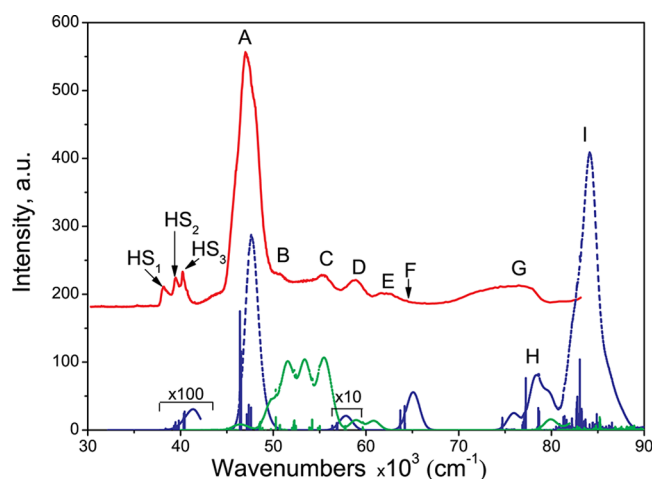


**Figure 13.** Measured excitation and simulated  $4f-5d$  absorption spectra of  $\text{Tb}^{3+}$  ions in  $\text{K}_3\text{YF}_6$ .

The host absorption and CT transition, respectively, with the predicted onset at  $\sim 87\,000\text{ cm}^{-1}$  and  $81\,000\text{ cm}^{-1}$  are not observed, but they generally play a role of competing with the  $4f-5d$  transition so that some  $4f-5d$  transition bands around their energy positions might not be observed. The first SA  $4f^8 \rightarrow 4f^76s$  transition band was predicted at  $\sim 75\,900\text{ cm}^{-1}$  by referring to the Table 5, which is consistent with the maximum at  $76\,187\text{ cm}^{-1}$  of the observed band G. As a caution, the origin of the band G still needs to be further confirmed in combination with the  $4f-5d$  transition assignments.

By referring to the predicted energy value of the lowest  $4f-5d$  SA transition of  $\text{Tb}^{3+}$  ions situated at the Y site in the Table 5, the band A with the maximum at  $47\,104\text{ cm}^{-1}$  is associated with the Y site and assigned to the SA transition to the low-energy  $5d$  CF component  $t_2$ . Comparison with the energy positions of the excitation bands of  $\text{Ce}^{3+}$  ions situated at the Y site shows that the band F with the maximum at  $64\,415\text{ cm}^{-1}$  corresponds to the SA transitions to the high-energy  $5d$  CF component  $e$ . It is no wonder that the CF splitting for  $\text{Tb}^{3+}$  is smaller than for  $\text{Ce}^{3+}$  due to the reduction of  $5d$  CF strength with the contraction of lanthanide ionic radii, as mentioned before. Following the simple model,<sup>91</sup> the bands A and F can be denoted as  ${}^7[{}^8S; {}^2t_2]$  and  ${}^7[{}^8S; {}^2e]$ . In addition to the excitation of the  $5d$  electron, the  $4f^7$  core of  $\text{Tb}^{3+}$  can also be excited from ground term  ${}^8S$  to excitation terms  ${}^6P$  or  ${}^6I$ . The term splittings  ${}^6P-{}^8S$  and  ${}^6I-{}^8S$  can be read from the energy structure of  $\text{Gd}^{3+}$



ions in Dieke's diagram and are, respectively,  $\sim 32\,500\text{ cm}^{-1}$  and  $\sim 36\,300\text{ cm}^{-1}$ . Thus, the energy positions of  ${}^7[{}^6P; {}^2t_2]$  and  ${}^7[{}^6I; {}^2t_2]$  are, respectively, expected at  $79\,600\text{ cm}^{-1}$  and  $83\,400\text{ cm}^{-1}$ , as the bands H and I show in Figure 13. However, the simulated band I can not be observed since the CT transition around the energy range is large. Moreover, the simulated band H does not also correspond to the band G. This is because the bandwidth of the simulated band H does not agree with the real bandwidth (about  $8000\text{ cm}^{-1}$ ) of the broad band G without any fine structure. The former usually has very small bandwidth and the fine structure due to the 5d electron being in the ground 5d CF component, as pointed out by ref 93. Thus, the band G was assigned as the first SA  $4f\text{--}6s$  transition, and the tail of the band G might include the transition to  ${}^7[{}^6I; {}^2t_2]$ . This band structure character at this energy in  $\text{K}_3\text{YF}_6$  is different from that in other fluoride hosts, such as  $\text{LiYF}_4$ <sup>21</sup> and  $\text{Cs}_2\text{NaYF}_6$ ,<sup>22</sup> where the states with  ${}^6P$  and  ${}^6I$  core components can be observed.

There are four observed bands with maxima at  $51\,028\text{ cm}^{-1}$  (B),  $55\,392\text{ cm}^{-1}$  (C),  $58\,825\text{ cm}^{-1}$  (D), and  $61\,472\text{ cm}^{-1}$  (E) between the bands A and F. They would be attributed as the K(1) site since there is no SA band of the Y site to be found in the range from bands A to F. After comparing with the 5d CF splitting of  $\text{Ce}^{3+}$  ions situated at the K(1) site, the bands B–E, respectively, correspond to the SA transitions to the first, third, fourth, and fifth 5d CF components as shown by our simulated vibronic bands and can be denoted as  ${}^7[{}^8S; {}^2\Gamma_i]$  ( $i = 1, 3, 4, 5$ ) where  $\Gamma_i$  is the irreducible representation of the  $i$ th 5d CF components. The high energy  ${}^7[{}^6P; {}^2\Gamma_i]$  and  ${}^7[{}^6I; {}^2\Gamma_i]$  of the K(1) site are always buried by those of the Y site as shown by our CF calculations, and thus can not be observed in the excitation spectrum.

For the heavy  $\text{Ln}^{3+}$  ions, both SF and SA  $4f\text{--}5d$  transitions can be observed since the fact that the HS state is always lying below the LS state results in that the weak SF transition can not be buried by the strong SA transition. The first  $4f\text{--}5d$  SF transition band around  $40\,000\text{ cm}^{-1}$  belonging to the Y site is observed and can be assigned as  ${}^9[{}^8S; {}^2t_2]$ . It consists of three ZPLs, respectively, at  $38\,158\text{ cm}^{-1}$  ( $\text{HS}_1$ ),  $39\,230\text{ cm}^{-1}$  ( $\text{HS}_2$ ), and  $40\,275\text{ cm}^{-1}$  ( $\text{HS}_3$ ). This fine energy splitting is very similar to that in  $\text{Cs}_2\text{NaYCl}_6$ .<sup>94</sup> It can be understood as the effect induced by the 5d electron spin–orbit coupling interaction because the 4f core spin–orbit coupling interaction does not cause any energy splitting for the  $4f^75d$  transition final states with  ${}^8S$  core quantum numbers due to the quenching of the total orbit angular momentum of the  ${}^8S$  term of  $4f^7$  core. The detailed explanation of the triplex splitting can be found in our previous work.<sup>95</sup> On the basis of the position estimation of the ZPL of the band A, the energy separation between the first SF and SA  $4f\text{--}5d$  transitions of  $\text{Tb}^{3+}$  in  $\text{K}_3\text{YF}_6$  (i.e.,  $\text{ZPL(A)}\text{--}\text{HS}_1$ ) is estimated as  $7776\text{ cm}^{-1}$ , similar to the splitting between the first HS and LS states observed in  $\text{LiYF}_4\text{:Tb}^{3+}$ .<sup>21</sup> According to this splitting, the energy position of the second  $4f\text{--}5d$  SF transition band belonging to the Y site can be determined from the band F and thus is located at  $57\,702\text{ cm}^{-1}$ . The same procedure was applied to the first  $4f\text{--}5d$  SF transition band belonging to the K(1) site. Its energy position was placed at  $46\,510\text{ cm}^{-1}$ . Since these SF transitions both fall into the nearest SA bands, they can not be observed in the excitation spectrum.

The theoretical simulations show the better consistence with the experimental excitation spectrum, as shown in Figure 13, where the calculated absorption intensities of the first and second  $4f\text{--}5d$  SF transition bands belonging to the Y site were enlarged for better display, respectively, by 100 and 10 times.

**Dy<sup>3+</sup>.** Figure 14 shows the excitation spectrum of  $\text{Dy}^{3+}$  ions doped in  $\text{K}_3\text{YF}_6$  monitoring the  ${}^4F_{9/2} \rightarrow {}^6H_{13/2}$  emission at  $579$

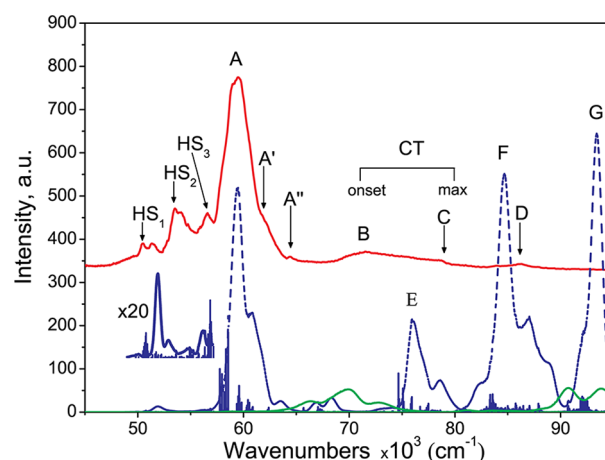


**Figure 14.** Measured excitation and simulated  $4f\text{--}5d$  absorption spectra of  $\text{Dy}^{3+}$  ions in  $\text{K}_3\text{YF}_6$ .

nm. The host absorption is not observed in the excitation spectrum. The CT transition is expected at  $\sim 80\,200\text{ cm}^{-1}$  according to the prediction in Table 5. The band C with the maximum at  $78\,821\text{ cm}^{-1}$  seems to be attributed as this mechanism. However, the weak intensity of the band C and the bandwidth being not as broad as the possible range of CT transition implies, the band might not correspond to CT transition. The  $4f^9 \rightarrow 4f^86s$  transition was predicted at  $\sim 83\,200\text{ cm}^{-1}$ , not very close to the band D with the maximum at  $85\,856\text{ cm}^{-1}$ . It is very arbitrary to directly assign the band D to the  $4f\text{--}6s$  transition.

By referring to the predicted energy value of the lowest  $4f\text{--}5d$  SA transition of  $\text{Dy}^{3+}$  ions situated at the Y site in Table 5, the band A with the maximum at  $59\,447\text{ cm}^{-1}$  is associated with the Y site and assigned to the first SA transition  ${}^6[{}^7F; {}^2t_2]$ . Comparison with the energy positions of the excitation bands of  $\text{Ce}^{3+}$  ions situated at the Y site shows the next possible SA transition to  ${}^6[{}^7F; {}^2e]$  is expected at  $\sim 78\,100\text{ cm}^{-1}$ , which is very close to the simulated band E and the observed band C. Thus, the band C was assigned to the second SA transition to  ${}^6[{}^7F; {}^2e]$  of the Y site, whose intensity is obviously weakened by the CT transition. The  $4f^8$  core can also be excited from ground term  ${}^7F$  to high-energy terms  ${}^5D$  and  ${}^5G$ , whose energy positions relative to  ${}^7F$  can be read from the energy structure of  $4f^8$  configuration of  $\text{Tb}^{3+}$  ion in Dieke's diagram, and are, respectively,  $\sim 25\,300$  and  $\sim 34\,100\text{ cm}^{-1}$ . The higher energy  ${}^6[{}^5D; {}^2t_2]$  and  ${}^6[{}^5G; {}^2t_2]$  will be placed at  $\sim 84\,700$  and  $\sim 93\,500\text{ cm}^{-1}$ , as the simulated bands F and G show. The latter is not observed due to the prevention of the host absorption. The former is around the band D. Thus, the band D was assigned to the third SA transition to  ${}^6[{}^5D; {}^2t_2]$  of the Y site, whose intensity becomes very low due to the competitive behavior of the  $4f\text{--}6s$  transition. Our CF calculations for the Y site show the possible splitting of  ${}^6[{}^7F; {}^2t_2]$  (i.e., band A) ends at  $70\,000\text{ cm}^{-1}$ , and thus, the band B with the maximum at  $71\,323\text{ cm}^{-1}$  might not be associated with the Y site but the K(1) site. The CF calculations for the K(1) site support the conclusion, as shown in the Figure 14. The much larger bandwidth of band B almost equal to  $10\,000\text{ cm}^{-1}$  reflects that band B is not formed alone by some transition mechanism but the result of joint



actions by the 4f–5d transitions of the Y and K(1) sites and CT transition.

There are two peaks marked with A' and A'', respectively, at 61 803 and 64 492  $\text{cm}^{-1}$ . This is mainly because of the splitting of  $^6[{}^7\text{F}; {}^2\text{t}_2]$  caused by the 4f core and 5d spin–orbit coupling interactions. It is hard to construct one intuitive physics picture to understand the further splitting because the mixing of various quantum numbers caused by various comparable interactions is too strong to construct the approximate eigenstates for  $\text{Dy}^{3+}$  ion, as the complication was shown in the simple model calculation carried out in ref 96. The present programmed calculations have revealed the positions of peaks A' and A'' (see Figure 14). The first group of the SF transition bands is observed around 53 000  $\text{cm}^{-1}$  and can be assigned as  $^8[{}^7\text{F}; {}^2\text{t}_2]$ . It consists of three ZPLs, respectively, at 50 519  $\text{cm}^{-1}$  ( $\text{HS}_1$ ), 53 466  $\text{cm}^{-1}$  ( $\text{HS}_2$ ), and 56 467  $\text{cm}^{-1}$  ( $\text{HS}_3$ ), and the related vibronic sideband. The energy separations between the three ZPLs are very similar to that reported in  $\text{LiYF}_4\text{:Dy}^{3+}$ .<sup>21</sup> This is similar because of the splitting induced by the 4f core and 5d spin–orbit coupling interactions. On the basis of the position estimation of the ZPL of band A, the energy separation between the first SF and SA 4f–5d transitions of  $\text{Dy}^{3+}$  in  $\text{K}_3\text{YF}_6$  (i.e.,  $\text{ZPL(A)}-\text{HS}_1$ ) is estimated as 7758  $\text{cm}^{-1}$ , which is also similar to the splitting between the first HS and LS states observed in  $\text{LiYF}_4\text{:Dy}^{3+}$ .<sup>21</sup>

The theoretical simulations agree with the experimental excitation spectrum very well, where the calculated absorption intensities of the first 4f–5d SF transition bands belonging to the Y site were enlarged for better display by 20 times. In addition, the calculated 4f<sup>8</sup>5d levels start at 47 946  $\text{cm}^{-1}$ , which also agrees with the onset of the observed peak  $\text{HS}_1$ .

**Er<sup>3+</sup>.** Figure 15 shows the excitation spectrum of  $\text{Er}^{3+}$  ions doped in  $\text{K}_3\text{YF}_6$  monitoring the  ${}^4\text{S}_{3/2} \rightarrow {}^4\text{I}_{15/2}$  emission at 552

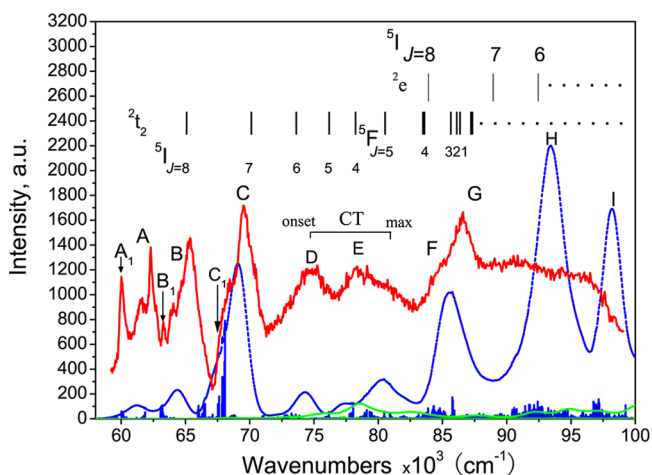


**Figure 15.** Measured excitation and simulated 4f–5d absorption spectra of  $\text{Er}^{3+}$  ions in  $\text{K}_3\text{YF}_6$ .

nm. At the high-energy direction, the last broad band G starts at 86 531  $\text{cm}^{-1}$  and reaches the maximum at 87 887  $\text{cm}^{-1}$ . According to the previously observed feature of the host absorption in the excitation spectra of other  $\text{Ln}^{3+}$  ions, the band G was unambiguously assigned to the host absorption. The maxima of the CT transition and first SA  $4\text{f}^{11} \rightarrow 4\text{f}^{10}6\text{s}$  transition was predicted at  $\sim 81\,900$  and  $\sim 83\,600$   $\text{cm}^{-1}$  by referring to Table 5. It looks that the bands E and F can be, respectively, attributed as the CT transition and first SA 4f–6s

transition, as shown in the Figure 15. However, the bandwidth of the band E is not the same as the possible range of the CT transition marked in the Figure 15. Moreover, the abundant vibronic structure of the band F is also very different from the previously observed feature of the first SA 4f–6s transition in the excitation spectra of other  $\text{Ln}^{3+}$  ions. Thus, this suggests the bands E and F might originate from the 4f–5d transitions.

$\text{Er}^{3+}$  ion is a very close match in ionic radius for  $\text{Y}^{3+}$  ion, as shown in Table 1. This means most  $\text{Er}^{3+}$  ions go into the Y sites, and the possibility of occupying the K(1) sites becomes very small. In addition, the further CF calculations show that the simulated absorption spectrum of the K(1) site (the green dotted line) is always buried by that of the Y site (the blue dashed line), as shown in Figure 15. Thus, all the broad bands in the excitation spectrum were thought to be associated with the Y site. The six broad bands associated with 4f–5d transitions are observed with the maxima at 61 402  $\text{cm}^{-1}$  (A), 65 092  $\text{cm}^{-1}$  (B), 69 092  $\text{cm}^{-1}$  (C), 74 376  $\text{cm}^{-1}$  (D), 78 442  $\text{cm}^{-1}$  (E), and 84 757  $\text{cm}^{-1}$  (F). The first three bands show fine structure, and their ZPLs are, respectively, located at 59 983  $\text{cm}^{-1}$  ( $\text{A}_1$ ), 63 081  $\text{cm}^{-1}$  ( $\text{B}_1$ ), and 68 083  $\text{cm}^{-1}$  ( $\text{C}_1$ ). The calculated 4f<sup>8</sup>5d levels start at 57 182  $\text{cm}^{-1}$ , not very far away from  $\text{A}_1$ .

Since the 4f–5d Coulomb interaction begins to become weaker than the 4f core spin–orbit coupling interaction for  $\text{Er}^{3+}$  ions, Duan and Xia et al.<sup>70</sup> suggested that the energy structure of the 4f<sup>10</sup>5d configuration of  $\text{Er}^{3+}$  ion can be approximately regarded as the HS and LS splitting induced by the 4f–5d Coulomb interaction upon the basis of the supposition of the multiplets of the 4f<sup>10</sup> core ( ${}^{2S+1}\text{L}_{\text{qf}}$ ) and 5d CF components. For our case, the following symbols [ ${}^{2S+1}\text{L}_{\text{qf}}; {}^2\Gamma_{\text{d}}\text{HS}$ ] and [ ${}^{2S+1}\text{L}_{\text{qf}}; {}^2\Gamma_{\text{d}}\text{LS}$ ] were employed where  $\Gamma_{\text{d}} = \text{t}_2$  or e,  $\text{HS} = J_{\text{f}} + 1/2$ , and  $\text{LS} = J_{\text{f}} - 1/2$ . By referring to the predicted energy value of the lowest 4f–5d SA transition of  $\text{Er}^{3+}$  ions in Table 5 and the ground multiplet of 4f<sup>10</sup> configuration, the band B corresponds to the first SA transition and is assigned as [ ${}^5\text{I}_8; {}^2\text{t}_2$ ]<sub>15/2</sub>. To fairly well show the positions of all the SA transition bands, the two sets of the energy structures of 4f<sup>10</sup> configuration of  $\text{Ho}^{3+}$  ion doped in the  $\text{LaF}_3$  generated by free ion calculation using the free ion parameters reported in ref 17 were plotted in Figure 15, where the energy position of [ ${}^5\text{I}_8; {}^2\text{t}_2$ ]<sub>15/2</sub> was set at the maximum of the band B; the energy position of [ ${}^5\text{I}_8; {}^2\text{e}$ ]<sub>15/2</sub> can be approximately determined by referring to the energy difference between the first and fifth CF components of  $\text{Ce}^{3+}$  ion situated at the Y site in Table 8; [ ${}^{2S+1}\text{L}_{\text{qf}}; {}^2\Gamma_{\text{d}}\text{LS}$ ] with energies exceeding over the energy of the host absorption edge will be discarded. By inspecting the position of [ ${}^{2S+1}\text{L}_{\text{qf}}; {}^2\Gamma_{\text{d}}\text{LS}$ ] shown in Figure 15, the bands C, D, E, and F can be, respectively, explained as four SA transitions to [ ${}^5\text{I}_7; {}^2\text{t}_2$ ]<sub>13/2</sub>, [ ${}^5\text{I}_6; {}^2\text{t}_2$ ]<sub>11/2</sub>, [ ${}^5\text{I}_4; {}^2\text{t}_2$ ]<sub>7/2</sub>, and [ ${}^5\text{I}_8; {}^2\text{e}$ ]<sub>15/2</sub>. The state [ ${}^5\text{F}_4; {}^2\text{t}_2$ ]<sub>7/2</sub> has also the contribution to the band F. In addition, the excitation curves between the ranges of D–E and E–F are not very smooth. This means the excitations of D–E and E–F might be assigned to the transitions to [ ${}^5\text{I}_5; {}^2\text{t}_2$ ]<sub>9/2</sub> and [ ${}^5\text{F}_5; {}^2\text{t}_2$ ]<sub>9/2</sub>. Finally, the band A was assigned as the first SF transition to [ ${}^5\text{I}_8; {}^2\text{t}_2$ ]<sub>17/2</sub>. The energy separation between the first SF and SA 4f–5d transitions of  $\text{Er}^{3+}$  in  $\text{K}_3\text{YF}_6$  ( $\text{B}_1-\text{A}_1$ ) is estimated as 3098  $\text{cm}^{-1}$ , which is also similar to the splitting between the first HS and LS states observed in  $\text{LiYF}_4\text{:Er}^{3+}$ .<sup>21</sup> The intensity of the band A is not as weak as the first 4f–5d SF transitions of  $\text{Tb}^{3+}$  and  $\text{Dy}^{3+}$  ions in the same host since the 5d spin–orbit

coupling interaction can effectively mix  $[^5I_8; ^2t_{2}]_{17/2}$  and  $[^5I_8; ^2t_{2}]_{15/2}$  states due to their small energy separation. The further detailed interpretation about the mechanism can be found in the ref 97.

The theoretical simulations agree with the experimental excitation spectrum very well. The simulated band H and I can be ignored due to the host absorption preventing their observations. It is seen from Figure 15 that the CT transition does not weaken the excitation efficiency of the 4f–5d transitions around them. This might be because the energy transfer efficiency to the luminescent energy level of  $\text{Er}^{3+}$  from the CT final states is less than that from the  $4f^{10}5d$  final states even though the absorption efficiency of the CT final states is stronger than that of the  $4f^{10}5d$  final states.

## CONCLUSIONS

The  $\text{K}_3\text{YF}_6$  host doped samples with trivalent rare earth ions ( $\text{Ce}^{3+}$ ,  $\text{Pr}^{3+}$ ,  $\text{Nd}^{3+}$ ,  $\text{Eu}^{3+}$ ,  $\text{Gd}^{3+}$ ,  $\text{Tb}^{3+}$ ,  $\text{Dy}^{3+}$  and  $\text{Er}^{3+}$ ) have been grown in a polycrystalline form and studied spectroscopically using synchrotron radiation. The excitation spectra of characteristic emission of rare earth ions were recorded in the VUV region at 8 K. Analysis of the obtained spectra was performed in the framework of the crystal field theory, namely, the combination of the exchange charge model of crystal field (which takes into account the actual symmetry of the crystal lattice and enables to calculate the crystal field parameters with taking into account the overlap effects between impurity ions and nearest neighbors) and extended f-shell programs (which enables to calculate the eigenvalues of the crystal field Hamiltonian in the extended basis set comprising two different electronic configurations ( $4f^N$  and  $4f^{N-1}5d$ ) and the transition intensities). From the calculated energy levels and spectra, a suggestion is proposed that the impurity ions occupy two possible positions in  $\text{K}_3\text{YF}_6$ : the Y and K(1) sites. Both sides are 6-fold coordinated by the fluorine ions and have the  $C_i$  local symmetry. In the present work, we assumed that the RE ions can occupy both available sites in the studied hosts. This theoretical assumption has not yet been experimentally checked. For possible experimental ways of identification and description of the multisite RE spectra in crystals, the reader is referred to refs 98–102.

The excitation spectra are dominated by the  $4f^N$ – $4f^{N-1}5d$  transitions. However, the high-lying  $4f^N$ – $4f^{N-1}6s$  transitions also contribute to the spectra, and their inclusion improves considerably the agreement with the experimental spectra shapes. We propose also a unified set of the crystal field, intra- and interconfigurational, parameters, which gives a consistent description of the complete energy level schemes and excitation spectra of the trivalent lanthanides in  $\text{K}_3\text{YF}_6$ . The area of application of such a set is not, however, restricted to the case of  $\text{K}_3\text{YF}_6$  only: it can be used as an initial set for simulating the spectroscopic properties of trivalent lanthanides in similar fluorides as well.

Since positioning of the impurity's energy levels with respect to the band structure of a host material is of paramount importance for possible applications, the energy level diagram, which includes the lowest states of the levels of the  $4f^N$ ,  $4f^{N-1}5d$ , and  $4f^{N-1}6s$  configurations of rare earth ions and lowest ligand–impurity ion charge transfer transitions superimposed onto the  $\text{K}_3\text{YF}_6$  electronic band structure, was plotted and analyzed. Such a diagram gives a very valuable insight into the electronic and optical properties of the chosen crystal and rare earth dopants.

The approach proposed in the present article to deal with the interconfigurational transitions of the trivalent lanthanide ions can be applied straightforwardly to other systems.

## AUTHOR INFORMATION

### Corresponding Author

\*E-mail: brik@fi.tartu.ee (M.G.B.); marek.gusowski@wp.pl (M.A.G.).

### Notes

The authors declare no competing financial interest.

## ACKNOWLEDGMENTS

C.-G.M. acknowledges financial supports from European Social Fund Grant GLOFY054MJD, Estonian Science Foundation Grants 7456, 6999, 6658, and 7612, and National Science Foundation of China under Grant 11204393. M.G.B.'s research was supported by European Social Fund's Doctoral Studies and Internationalisation Programme DoRa. M.A.G. and H.C.S. would like to acknowledge the beam-time allocation at Superlumi, DESY, Hamburg, within the project I-20100034. They would like to also thank for the support of the South African National Research Foundation (NRF) as well as the Material and Nano Science Cluster fund of the University of the Free State. We would like to thank Professor M.F. Reid for the use of his suite of software for f-shell system.

## REFERENCES

- (1) Jüstel, T.; Nikol, H.; Ronda, C. *Angew. Chem., Int. Ed.* **1998**, *37*, 3084–3103.
- (2) Xie, R.-J.; Hirosaki, N.; Sakuma, K.; Yamamoto, Y.; Mitomo, M. *Appl. Phys. Lett.* **2004**, *84*, 5404–5406.
- (3) Wegh, R. T.; Donker, H.; Oskam, K. D.; Meijerink, A. *Science* **1999**, *283*, 663–666.
- (4) Meijerink, A.; Wegh, R. T.; Vergeer, P.; Vlugt, T. *Opt. Mater.* **2006**, *28*, 575–581.
- (5) Joubert, M. F.; Guyot, Y.; Jacquier, B.; Chaminade, J. P.; Garcia, A. *J. Fluorine Chem.* **2001**, *107*, 235–240.
- (6) Pepin, C. M.; Berard, P.; Perrot, A. L.; Pepin, C.; Houde, D.; Lecomte, R.; Melcher, C. L.; Dautet, H. *IEEE Trans. Nucl. Sci.* **2004**, *51*, 789–795.
- (7) van Loef, E. V. D.; Dorenbos, P.; van Eijk, C. W. E.; Krämer, K. W.; Güdel, H. U. *Nucl. Instrum. Methods Phys. Res., Sect. A* **2002**, *486*, 254–258.
- (8) Khaidukov, N. M.; Kirm, M.; Lam, S. K.; Lo, D.; Makhov, V. N.; Zimmerer, G. *Opt. Commun.* **2000**, *184*, 183–193.
- (9) Tanner, P. A.; Duan, C.-K.; Makhov, V. N.; Kirm, M.; Khaidukov, N. M. *J. Phys.: Condens. Matter* **2009**, *21*, 395504.
- (10) Gusowski, M. A.; Gagor, A.; Trzebiatowska-Gusowska, M.; Ryba-Romanowski, W. *J. Solid State Chem.* **2006**, *179*, 3145–3150.
- (11) Gusowski, M. A.; Ryba-Romanowski, W. *J. Phys. Chem. C* **2008**, *112*, 14196–14201.
- (12) Gusowski, M. A.; Ryba-Romanowski, W. *Opt. Lett.* **2008**, *33*, 1786–1788.
- (13) Schiffbauer, D.; Wickleder, C.; Meyer, G.; Kirm, M.; Stephan, M.; Schmidt, P. C. *Z. Anorg. Allg. Chem.* **2005**, *631*, 3046–3052.
- (14) Buñuel, M. A.; Moine, B.; Jacquier, B.; Garcia, A.; Chaminade, J. P. *J. Appl. Phys.* **1999**, *86*, 5045–5053.
- (15) Putaj, P.; de Haas, J. T. M.; Krämer, K. W.; Dorenbos, P. *IEEE Trans. Nucl. Sci.* **2010**, *57*, 1675–1681.
- (16) Francini, R.; Grassano, U. M.; Landi, L.; Scacco, A.; D'Elena, M.; Nikl, M.; Cechova, N.; Zema, N. *Phys. Rev. B* **1997**, *56*, 15109–15114.
- (17) Carnall, W. T.; Goodman, G. L.; Rajnak, K.; Rana, R. S. *J. Chem. Phys.* **1989**, *90*, 3443–3457.
- (18) Wybourne, B. G. *Spectroscopic Properties of Rare Earths*; John Wiley & Sons, Inc.: New York, 1965.

- (19) Reid, M. F.; van Pieterse, L.; Wegh, R. T.; Meijerink, A. *Phys. Rev. B* **2000**, *62*, 14744–14749.
- (20) van Pieterse, L.; Reid, M. F.; Wegh, R. T.; Soverna, S.; Meijerink, A. *Phys. Rev. B* **2002**, *65*, 045113.
- (21) van Pieterse, L.; Reid, M. F.; Burdick, G. W.; Meijerink, A. *Phys. Rev. B* **2002**, *65*, 045114.
- (22) Duan, C.-K.; Tanner, P. A.; Meijerink, A.; Babin, V. J. *Phys.: Condens. Matter* **2009**, *21*, 395501.
- (23) Tanner, P. A.; Duan, C.-K.; Cheng, B.-M. *Spectrosc. Lett.* **2010**, *43*, 431–445.
- (24) Dorenbos, P. J. *Lumin.* **2000**, *91*, 91–106.
- (25) Dorenbos, P. J. *Lumin.* **2000**, *91*, 155–176.
- (26) Dorenbos, P. J. *Lumin.* **2005**, *111*, 89–104.
- (27) Dorenbos, P. J. *Phys.: Condens. Matter* **2003**, *15*, 8417.
- (28) Elias, L. R.; Heaps, W. S.; Yen, W. M. *Phys. Rev. B* **1973**, *8*, 4989–4995.
- (29) Moses, W. W.; Derenzo, S. E.; Weber, M. J.; Ray-Chaudhuri, A. K.; Cerrina, F. J. *Lumin.* **1994**, *59*, 89–100.
- (30) Dujardin, C.; Pedrini, C.; Garnier, N.; Belsky, A. N.; Lebbou, K.; Ko, J. M.; Fukuda, T. *Opt. Mater.* **2001**, *16*, 69–76.
- (31) Kirikova, N. Y.; Kirm, M.; Krupa, J. C.; Makhov, V. N.; Negodin, E.; Gesland, J. Y. *J. Lumin.* **2004**, *110*, 135–145.
- (32) Malkin, B. Z. In *Spectroscopy of Solids Containing Rare Earth Ions*; Kaplyanskiy, A. A., Macfarlane, R. M., Eds.; North-Holland Publishing Company (Elsevier): Amsterdam, The Netherlands, 1987; Chapter 2, p 13.
- (33) Shannon, R. D. *Acta Crystallogr., Sect. A: Found. Crystallogr.* **1976**, *32*, 751–767.
- (34) Zimmerer, G. *Radiat. Meas.* **2007**, *42*, 859–864.
- (35) Berkowitz, J. K.; Olsen, J. A. *J. Lumin.* **1991**, *50*, 111–121.
- (36) Hölsä, J.; Lamminmäki, R. J. *J. Lumin.* **1996**, *69*, 311–317.
- (37) Duan, C.-K.; Tanner, P. A. *J. Phys. Chem. A* **2010**, *114*, 6055–6062.
- (38) Auzel, F.; Malta, O. L. *J. Phys.* **1983**, *44*, 201–206.
- (39) Auzel, F. *J. Lumin.* **2001**, *93*, 129–135.
- (40) Duan, C.-K.; Tanner, P. A.; Babin, V.; Meijerink, A. *J. Phys. Chem. C* **2009**, *113*, 12580–12585.
- (41) Duan, C.-K.; Zhang, Y.; Ma, C.-G.; Xie, G.-Y.; Hu, L.-S. *J. Rare Earths* **2010**, *28*, 258–261.
- (42) Reid, M. F.; van Pieterse, L.; Meijerink, A. *J. Alloys Compd.* **2002**, *344*, 240–245.
- (43) Reid, M. F.; Duan, C.-K.; Zhou, H.-W. *J. Alloys Compd.* **2009**, *488*, 591–594.
- (44) Hu, L.-S.; Reid, M. F.; Duan, C.-K.; Xia, S.-D.; Yin, M. *J. Phys.: Condens. Matter* **2011**, *23*, 045501.
- (45) Brik, M. G.; Avram, N. M. *J. Phys. Chem. Solids* **2006**, *67*, 1599–1604.
- (46) Ning, L.-X.; Ying, J.; Xia, S.-D.; Tanner, P. A. *J. Phys.: Condens. Matter* **2003**, *15*, 7337.
- (47) Liu, G.-K.; Chen, X.-Y.; Huang, J. *Mol. Phys.* **2003**, *101*, 1029.
- (48) Malkin, B. Z.; Solov'yev, O. V.; Malishev, A. Y.; Saikin, S. K. *J. Lumin.* **2007**, *125*, 175–183.
- (49) Malkin, B. Z.; Pukhov, K. K.; Saikin, S. K.; Baibekov, E. I.; Zakirov, A. R. *J. Mol. Struct.* **2007**, *838*, 170–175.
- (50) Popova, M. N.; Chukalina, E. P.; Malkin, B. Z.; Saikin, S. K. *Phys. Rev. B* **2000**, *61*, 7421–7427.
- (51) Bertina, S.; Barbara, B.; Giraud, R.; Malkin, B. Z.; Vanuynin, M. V.; Pominov, A. I.; Stolov, A. L.; Tkachuk, A. M. *Phys. Rev. B* **2006**, *74*, 184421.
- (52) Wang, W.; Liu, G.-K.; Brik, M. G.; Seijo, L.; Shi, D. *Phys. Rev. B* **2009**, *80*, 155120.
- (53) Rudowicz, C.; Gnutek, P.; Brik, M. G. *J. Rare Earths* **2009**, *27*, 627–632.
- (54) Liu, G.-K.; Li, S.-T.; Zhorin, V. V.; Loong, C. K.; Abraham, M. M.; Boatner, L. A. *J. Chem. Phys.* **1998**, *109*, 6800–6808.
- (55) Solov'yev, O. V.; Malkin, B. Z. *J. Mol. Struct.* **2007**, *838*, 176–181.
- (56) Kirm, M.; Stryganyuk, G.; Vielhauer, S.; Zimmerer, G.; Makhov, V. N.; Malkin, B. Z.; Solov'yev, O. V.; Abdulsabirov, R. Y.; Korableva, S. L. *Phys. Rev. B* **2007**, *75*, 075111.
- (57) Brik, M. G.; Sildos, I.; Kiisk, V. J. *Lumin.* **2011**, *131*, 396–403.
- (58) Omelkov, S. I.; Brik, M. G.; Kirm, M.; Pustovarov, V. A.; Kiisk, V.; Sildos, I.; Lange, S.; Lobanov, S. I.; Isaenko, L. I. *J. Phys.: Condens. Matter* **2011**, *23*, 105501.
- (59) Liu, G.-K. In *Spectroscopic Properties of Rare Earths in Optical Materials*; Liu, G.-K., Jacquier, B., Eds.; Tsinghua University Press and Springer-Verlag: Heidelberg, Germany, 2005; Chapter 1, p 42.
- (60) Sternheimer, R. M.; Blume, M.; Peierls, R. F. *Phys. Rev.* **1968**, *173*, 376–389.
- (61) Garcia, D.; Faucher, M. *Phys. Rev. B* **1984**, *30*, 1703–1707.
- (62) Starostin, N. V. In *Crystal Spectroscopy*; Kaminski, A. D., Molgensitl, Z. P., Civilidov, D. T., Eds.; Nauka: Moscow, 1976.
- (63) Clementi, E.; Roetti, C. *At. Data Nucl. Data Tables* **1974**, *14*, 177–478.
- (64) Sovers, O. J. *J. Phys. Chem. Solids* **1967**, *28*, 1073–1074.
- (65) Edvardsson, S.; Klintenberg, M. *Mater. Sci. Forum* **1999**, *315*, 407–414.
- (66) Tanner, P. A.; Kumar, V. V. R. K.; Jayasankar, C. K.; Reid, M. F. *J. Alloys Compd.* **1994**, *215*, 349–370.
- (67) Görller-Walrand, C.; Binnemans, K. In *Handbook on the Physics and Chemistry of Rare Earths*; Gschneidner, K. A., Jr., Eyring, L., Eds.; North-Holland Publishing Company (Elsevier): Amsterdam, The Netherlands, 1996; Vol. 23, Chapter 155, p 199.
- (68) Ma, C.-G.; Brik, M. G.; Kiisk, V.; Kangur, T.; Sildos, I. *J. Alloys Compd.* **2011**, *509*, 3441–3451.
- (69) van Pieterse, L.; Heeroma, M.; de Heer, E.; Meijerink, A. *J. Lumin.* **2000**, *91*, 177–193.
- (70) Duan, C.-K.; Xia, S.; Reid, M. F.; Ruan, G. *Phys. Status Solidi B* **2005**, *242*, 2503–2508.
- (71) Peijzel, P. S.; Meijerink, A.; Wegh, R. T.; Reid, M. F.; Burdick, G. W. *J. Solid State Chem.* **2005**, *178*, 448–453.
- (72) Wegh, R. T.; Meijerink, A. *Phys. Rev. B* **1999**, *60*, 10820–10830.
- (73) Wegh, R. T.; Meijerink, A.; Lamminmäki, R. J.; Hölsä, J. *J. Lumin.* **2000**, *87–89*, 1002–1004.
- (74) Reid, M. F. In *Spectroscopic Properties of Rare Earths in Optical Materials*; Liu, G.-K., Jacquier, B., Eds.; Tsinghua University Press and Springer-Verlag: Heidelberg, Germany, 2005; Chapter 2, p 530.
- (75) Cowan, R. D. *The Theory of Atomic Structure and Spectra*; University of California Press: Berkeley, CA, 1981.
- (76) Hurtubise, V.; Freed, K. F. *J. Chem. Phys.* **1994**, *100*, 4955–4968.
- (77) Judd, B. R. *Phys. Rev.* **1962**, *127*, 750–761.
- (78) Ofelt, G. S. *J. Chem. Phys.* **1962**, *37*, 511–520.
- (79) Dorenbos, P. *Phys. Rev. B* **2000**, *62*, 15640–15649.
- (80) Brik, M. G. *J. Alloys Compd.* **2008**, *454*, 38–45.
- (81) Dujardin, C.; Pedrini, C.; Gâcon, J. C.; Petrosyan, A. G.; Belsky, A. N.; Vasil'ev, A. N. *J. Phys.: Condens. Matter* **1997**, *9*, S229.
- (82) Pedrini, C.; Joubert, M. F.; McClure, D. S. *J. Lumin.* **2007**, *125*, 230–237.
- (83) Takahashi, H.; Sakai, M.; Ono, S.; Sarukura, N.; Sato, H.; Fukuda, T. *Jpn. J. Appl. Phys.* **2003**, *42*, L660–L662.
- (84) Aull, B. F.; Jenssen, H. P. *Phys. Rev. B* **1986**, *34*, 6647–6655.
- (85) Vedrine, A.; Besse, J.; Baud, G.; Capestan, M. *Rev. Chim. Miner.* **1970**, *7*, 593.
- (86) Kodama, N.; Yamaga, M.; Henderson, B. *J. Appl. Phys.* **1998**, *84*, S820–S822.
- (87) Combes, C. M.; Dorenbos, P.; van Eijk, C. W. E.; Krämer, K. W.; Güdel, H. U. *J. Lumin.* **1999**, *82*, 299–305.
- (88) Kück, S.; Sokólska, I.; Henke, M.; Döring, M.; Scheffler, T. *J. Lumin.* **2003**, *102–103*, 176–181.
- (89) Ning, L.-X.; Duan, C.-K.; Xia, S.-D.; Reid, M. F.; Tanner, P. A. *J. Alloys Compd.* **2004**, *366*, 34–40.
- (90) Xia, S.-D.; Duan, C.-K.; Deng, Q.; Ruan, G. *J. Solid State Chem.* **2005**, *178*, 2643–2646.
- (91) Duan, C.-K.; Reid, M. F. *J. Solid State Chem.* **2003**, *171*, 299–303.

- (92) Burdick, G. W.; Burdick, A.; Deev, V.; Duan, C.-K.; Reid, M. F. *J. Lumin.* **2006**, *118*, 205–219.
- (93) van Pieterson, L.; Reid, M. F.; Meijerink, A. *Phys. Rev. Lett.* **2002**, *88*, 067405.
- (94) Ning, L.-X.; Mak, C. S. K.; Tanner, P. A. *Phys. Rev. B* **2005**, *72*, 085127.
- (95) Ma, C.-G.; Reid, M. F.; Duan, C.-K.; Xia, S.-D.; Yin, M. *J. Rare Earths* **2007**, *25*, 262–267.
- (96) Xia, S.-D.; Duan, C.-K. *Phys. Status Solidi B* **2006**, *243*, 2839–2846.
- (97) Ma, C.-G.; Jiang, S.; Duan, C.-K.; Yin, M.; Xia, S.-D. *Chin. Phys. B* **2009**, *18*, 1961–1967.
- (98) Wang, Y.; Liu, Y.; Xiao, Q.; Zhu, H.; Li, R.; Chen, X. *Nanoscale* **2011**, *3*, 3164.
- (99) Liu, Y.; Luo, W.; Li, R.; Liu, G.; Antonio, M. R.; Chen, X. *J. Phys. Chem. C* **2008**, *112*, 686–694.
- (100) Luo, W.; Li, R.; Liu, G.; Antonio, M. R.; Chen, X. *J. Phys. Chem. C* **2008**, *112*, 10370–10377.
- (101) Liu, Y.; Luo, W.; Li, R.; Zhu, H.; Chen, X. *Opt. Express* **2009**, *17*, 9748–9753.
- (102) Luo, W.; Fu, C.; Li, R.; Liu, Y.; Zhu, H.; Chen, X. *Small* **2011**, *7*, 3046–3056.